Journal of Quantitative Spectroscopy & Radiative Transfer 261 (2021) 107436

Contents lists available at ScienceDirect

Journal of Quantitative Spectroscopy & Radiative Transfer

journal homepage: www.elsevier.com/locate/jqsrt

# Excited state quantum phase transitions in the bending spectra of molecules

Jamil Khalouf-Rivera[a], Francisco Pérez-Bernal[a,b], Miguel Carvajal[a,b,*]

[a] Dpto. Ciencias Integradas, Facultad de Ciencias Experimentales, Centro de Estudios Avanzados en Física, Matemáticas y Computación, Unidad Asociada GIFMAN, CSIC-UHU, Universidad de Huelva, Spain
[b] Instituto Universitario Carlos I de Física Teórica y Computacional, Universidad de Granada, Spain

ARTICLE INFO

*Article history:*
Received 9 October 2020
Revised 13 November 2020
Accepted 14 November 2020
Available online 18 November 2020

*Keywords:*
Nonrigid molecules
Linear molecules
Excited state quantum phase transition
Bent molecules
Bending rovibrational structure
Algebraic vibron model

ABSTRACT

We present an extension of the Hamiltonian of the two dimensional limit of the vibron model to encompass all possible interactions up to four-body operators. We apply this Hamiltonian to the modeling of the bending spectrum of four molecules: HNC, $H_2S$, $Si_2C$, and NCNCS. The selected molecular species include linear, bent, and nonrigid equilibrium structures, proving the versatility of the algebraic approach which allows for the consideration of utterly different physical cases within a single Hamiltonian and a general formalism. For each case we compute predicted bending energies and wave functions, that we use to depict the associated quantum monodromy diagram, Birge-Sponer plot, and participation ratio. In nonrigid cases, we also show the bending energy functional obtained using the coherent –or intrinsic– state formalism.



## 1. Introduction

The two-dimensional nature of the vibrational bending degree of freedom, despite having the linear and bent molecular equilibrium structures physical limits, implies also rovibrational couplings in quasilinear systems that, even for triatomic systems, have been the source of frequent misunderstandings in the description of molecular bending dynamics [1]. If the potential energy surface associated with a particular system has its minimum in the origin (i.e. it coincides with the molecular axis) the system is said to be linear. If this minimum is replaced by a maximum, and the potential minimum is located somewhere else, the molecule is said to have a bent equilibrium structure. Of course, this is not always so simple –even for textbook examples with a linear configuration [2]– and, apart from the two well-defined limiting cases, one often has to deal with quasilinear molecules, whose bending dynamics is characterized by large amplitude nuclear displacements and are not well described within the traditional normal mode approach. The possible cases occurring for intermediate situations can be clearly illustrated by correlation energy diagrams that follow the evolution of energy levels from one limiting case to the other [3,4].

For quasilinear molecular species, we introduce in the present work a further distinction between *quasilinear* and *nonrigid* molecules. The quasilinear case has a molecular bending potential with a flat minimum at the origin, and its bending spectrum has peculiar signatures, e.g., a positive anharmonicity in the Birge-Sponer plot or an anomalous ordering of the energy levels –with maximum vibrational angular momentum levels at lower energies for a given number of quanta of vibration. The nonrigid case is even richer in spectroscopic signatures, and it happens in a system with a potential minimum that is not in the origin, once the bending excitation energy reaches values high enough to allow for the exploration by eigenstates of the linear configuration, which in principle is classically forbidden due to the existence of the barrier to linearity. This explains the switch between negative and positive anharmonicities in the Birge-Sponer plot that characterizes these molecules, the well-known Dixon dip [5]. Birge-Sponer plots obtained with the present model for the different cases described above, besides the limiting linear and bent configurations, can be found in Refs. [6–8].

The study of large amplitude bending dynamics, and the ensuing coupling between vibrational and rotational degrees of freedom, has been successfully carried out making use of different approaches. Most of them solve a zeroth-order Hamiltonian, where

* Corresponding author.
*E-mail addresses:* yamil.khalouf@dci.uhu.es (J. Khalouf-Rivera), francisco.perez@dfaie.uhu.es (F. Pérez-Bernal), miguel.carvajal@dfa.uhu.es (M. Carvajal).

https://doi.org/10.1016/j.jqsrt.2020.107436

the large amplitude motion (LAM) is placed on equal footing with rotations, and then consider the complete vibrational-rotational Hamiltonian with respect to a configuration of reference. Perfect examples of this philosophy are the bender Hamiltonian of Hougen-Bunker-Johns [9], its extensions, like the semirigid bender Hamiltonian [10] and the general semirigid bender Hamiltonian [11], or the MORBID [12] model. The consideration of both rotational and vibrational degrees of freedom makes these models extremely useful tools for the analysis of molecular spectra, as they allow for the modeling of experimental term values and the assignment of quantum labels.

The barrier to linearity in nonrigid species is often modeled with Mexican-hat type potentials. Classical mechanics show that such potentials prevent the definition of a set of globally valid action-angle variables [13]. When this situation is brought into the quantum mechanics realm, the lack of global action-angle variables translates into the impossibility of finding a unique set of vibrational quantum numbers globally valid for the system [14,15]. This phenomenon, called *quantum monodromy*, is explained by the changes experienced by the system spectrum as the linear configuration, initially forbidden, can be explored for increasing excitation energies. Introduced by Child, quantum monodromy is characterized by a piling of states around a critical energy value and a particular dependence of the bending energy levels on the vibrational angular momentum, evinced in the quantum monodromy diagram [14]. This feature was soon used as an effective tool for the labeling of highly-excited energy levels of water in particularly difficult energy regions [16]. Quantum monodromy signatures have been later found in other molecular species [15,17–21].

The present work is based on an algebraic approach that treats quantum many-body systems with $N$ degrees of freedom in terms of bosonic realizations of the $U(N+1)$ Lie algebra [22]; an approach that has been successfully applied to the modeling of the structure of widely different physical systems: nuclei [23,24], hadrons [25], and molecules [26]. In the latter case, rovibrational excitations in molecules are treated as collective bosonic excitations called *vibrons*, and the model is known as the *vibron model*. This approach was originally introduced by Iachello for the study of the full rovibrational spectrum of diatomic molecular species [27]. In the present paper, we use the two-dimensional limit of the vibron model (2DVM), with a $U(3)$ dynamical algebra, originally introduced for the study of single and coupled benders [28]. This model provides an effective Hamiltonian able to deal with large amplitude bending modes and including from the onset couplings with the rotational projection around the molecule-fixed z-axis. It allows for a simple, though complete, description of the linear and bent limiting cases, as well as of the quasilinear and nonrigid regimes [6,29]. A thorough description of the model can be found in Ref. [7].

A point of particular interest for algebraic models is the study of ground state quantum phase transitions (QPTs), also called shape phase transitions, that are zero-temperature transitions between phases associated with specific configurations of the system ground state. The different phases are often associated with well-known limits, called *dynamical symmetries* [30]. These transitions are non-thermal and are driven through the variation of one or several Hamiltonian parameters (control parameters). The study of such transitions can be traced back to the seminal studies of Gilmore [31] and it has received a great deal of attention in algebraic models of nuclear structure [32–34]. The description of the ground state QPT for the 2DVM model is found in Ref. [7], while different aspects of interest about this transition can be found in Refs. [35–40].

More recently, the ground state QPT concept has been extended to encompass excited states, with the introduction of excited state quantum phase transitions (ESQPTs). ESQPTs are characterized by a singularity in the energy spectrum due to the clustering of excited levels at a certain critical energy [41,42]. ESQPTs have been studied in different models, e.g., the nuclear interacting boson [32], Jaynes-Cummings [43], kicked-top [44], Rabi [45], Lipkin-Meshkov-Glick (LMG) [32,46–50], and Dicke [36,43,51,52] models. For a recent review see Ref. [53] and references therein.

In the molecular case, it was shown that quantum monodromy and its associated excited levels clustering can be understood as a manifestation of an ESQPT [7] and it can be described with a formulation common to other many-body systems [41,54,55]. Due to the advances in experimental techniques that have made feasible to record highly-excited bending overtones in nonrigid systems, the molecular bending degree of freedom has been the first quantum system where experimental signatures of ESQPTs have been identified [17,18] and explained from an algebraic perspective [8,56]. Other systems where experimental access to ESQPTs has been achieved are superconducting microwave billiards [57] and spinor condensates [58].

The present work can be considered as an extension and an update of the results presented in [8] and [56], with the main aim of calculating spectra within the 2DVM with uncertainties close to spectroscopic accuracy. In these two works, particular bending modes of several molecular species with different characteristics – linear, quasilinear, nonrigid, and bent– were modeled making use of the 2DVM. The selected species are mostly four- or five-atomic in [8] and triatomic in [56] and their bending rovibrational structure was explained in terms of the most general 2DVM Hamiltonian up to two-body interactions (besides the water molecule case, where extra interactions were taken into consideration). We extend the number of interactions and make use of the most general 2DVM Hamiltonian including up to four-body interactions. To illustrate the improved results achieved with this extension, we show results for four molecular species: hydrogen isocyanide (HNC, linear), hydrogen sulfide ($H_2S$, bent), cyanogen isothiocyanate (NCNCS, nonrigid), and disilicon carbide ($Si_2C$, nonrigid). We provide in the Supplementary Material section the predicted values for not yet measured levels as well as the residual plots for our fits.

In addition to the calculated spectra and spectroscopic parameters for the selected species, we have also computed the participation ratio [59] (PR) of the resulting eigenstates expressed in the two 2DVM bases, associated with the linear and bent limiting cases [7].

Finally, in nonrigid cases, we make use of the coherent or intrinsic state formalism [7,60,61] to compute an approximation to the system bending energy functional.

## 2. The two dimensional limit of the vibron model

The vibron model, based on the $U(4)$ Lie algebra, was originally devised for the study of diatomic molecular species [27]. This model was later extended to model the spectrum of tri- [62] and tetratomic [63] molecular species. The simultaneous treatment of all rotational and vibrational degrees of freedom comes at a cost, and the required coupling of $U(4)$ algebras increase the mathematical and computational complexity of the model.

As a possible way of overcoming this drawback, a simplified version, the 2D limit of the vibron model -abbreviated as 2DVM- was introduced to model molecular bending vibrations [28]. Since then, due to its general character, it has proved able to encompass the limiting linear and bent molecular structures, besides the interesting situations in-between them. In the field of molecular structure, the model was applied to different problems involving bending vibrations: calculation of infrared or Raman line intensities [29,64–68], definition of an algebraic force field for bending vibrations [69], computation of Franck-Condon factors [70], or characterizing signatures of non-rigidity in energy spectra [6,8,56].

More recently, the authors have found that the 2DVM model is capable of characterizing the transition state in such reactions, applying this finding to the bond-breaking system HCN-HNC [71].

In fact, as the 2DVM is the simplest two-level bosonic model with a non-trivial angular momentum, it has been often used to illustrate the occurrence of ESQPTs in algebraic models [42,72,73]. The authors and Santos have also recently shown clear evidences of a link between the ESQPT formalism and the study of the transition state in isomerization chemical reactions [71].

Alternative algebraic approaches to molecular structure that try to get a firmer grasp on the connection to the traditional phase space approach are also based on the 2DVM [74–76].

Specially important for the present discussion are the detailed description of the model provided in Ref. [7] and Refs. [8,56], where a careful study of many different benders is presented and the model results are explained under the prism of the occurrence of an ESQPT in nonrigid cases. Nonrigid molecules have vibrational bending levels that straddle the barrier to linearity, whose wavefunctions have significant components in both the linear and bent regions of configuration space, giving rise to particular spectroscopic signatures. The spectra of such molecules display features typical of a bent or linear configurations, depending on the energy window considered and they showcase the expected ESQPT precursors for a finite system, once the system overcomes the potential barrier and explores the previously forbidden linear configuration region of the phase space.

It is worth to mention the extension of the model to situations where two benders are coupled, which implies a significantly larger computational complexity [77,78] and where the obtained results can be explained from the perspective of QPTs involving two bosonic fluids [79–83]. Related to this, it is worth mentioning the use of the 2DVM model in the study of the spectra of 2D crystals with various lattice geometries [84].

The 2DVM associates a $U(3)$ dynamical algebra to each bender. The nine generators of this Lie algebra are built as bilinear products of a creation and an annihilation operator from the basic bricks for the algebra: two Cartesian bosons $(\tau_x, \tau_y)$ and a scalar boson $(\sigma)$. The system Hamiltonian is obtained as an expansion in terms of operators with the right symmetry properties that belong either to the dynamical algebra or to one of its subalgebras. The interested reader can find a detailed mathematical description of the model in Refs. [7,28]. We provide here some basic details concerning the bases and Hamiltonians we use in the present work and we also introduce the participation ratio, a quantity used to analyze the wave function localization in the different bases. We also outline the intrinsic state formalism, used to obtain the classical limit of the model in the mean field approximation.

### 2.1. The cylindrical and displaced oscillator bases

There are two possible subalgebra chains starting from the dynamical algebra, $U(3)$, and ending in the system symmetry algebra, $SO(2)$. The requirement of having $SO(2)$ as the symmetry algebra implies angular momentum conservation in the system [85].

$$\begin{array}{ccccc} & & U(2) & & Chain(I) \\ & \nearrow & & \searrow & \\ U(3) & & & & SO(2) \\ & \searrow & & \nearrow & \\ & & SO(3) & & Chain(II) \end{array} \tag{1}$$

Each one of the possible subalgebra chains is known as a *dynamical symmetry* and it provides an analytical solution to the problem: an energy formula that can be mapped to certain physical cases [22,85]. In addition to this, there is a basis associated with every dynamical symmetry. We proceed to detail the basis quantum numbers and branching rules for the two dynamical symmetries at stake.

*The cylindrical oscillator basis.* The $U(3) \supset U(2) \supset SO(2)$ chain is known as the cylindrical oscillator chain and it can be mapped with the linear case. Its states are labeled by quantum numbers $n$ and $\ell$

$$\left| \begin{array}{ccccc} U(3) & \supset & U(2) & \supset & SO(2) \\ [N] & & n & & \ell \end{array} \right\rangle, \tag{2}$$

and the associated basis states are denoted as $|[N]; n^{\ell}\rangle$. The quantum number $N$ labels the totally symmetric representation of $U(3)$ and the total number of bound states of the system is a function of $N$. The label $n$ is the vibrational quantum number and $\ell$ is the vibrational angular momentum. The branching rules in this case are

$$\begin{aligned} &n = N, N-1, N-2, \ldots, 0 \\ &\ell = \pm n, \pm(n-2), \ldots, \pm 1 \text{ or } 0 \quad (n = \text{odd or even}). \end{aligned} \tag{3}$$

This is the most convenient basis to fit vibrational bending data from linear molecules. We provide in A.0.1 the matrix elements in this basis of the different operators included in the 2DVM Hamiltonian.

*The displaced oscillator basis.* States in the displaced oscillator chain, associated with bending vibrations in molecules with a bent geometric configuration, are characterized by the quantum numbers

$$\left| \begin{array}{ccccc} U(3) & \supset & SO(3) & \supset & SO(2) \\ [N] & & \omega & & \ell \end{array} \right\rangle \tag{4}$$

and will be denoted as $|[N]; \omega, \ell\rangle$. The branching rules in this case are

$$\begin{aligned} &\omega = N, N-2, N-4, \ldots, 1 \text{ or } 0 \quad (N = \text{odd or even}), \\ &\ell = \pm\omega, \pm(\omega-1), \ldots, 0. \end{aligned} \tag{5}$$

It is convenient to introduce a vibrational quantum number $\nu_b$, which can be identified with the number of quanta of excitation in the displaced oscillator $\nu_b = \frac{N-\omega}{2}$. The branching rules in this case are

$$\begin{aligned} &\nu_b = 0, 1, \ldots, \frac{N-1}{2} \text{ or } \frac{N}{2} \quad (N = \text{odd or even}), \\ &K = \ell = 0, \pm 1, \pm 2, \ldots, \pm(N - 2\nu_b), \end{aligned} \tag{6}$$

expressed in terms of symmetric top quantum labels. This is the natural basis to fit bending vibration data from nonrigid and bent molecules. We provide in A.0.2 the values of the matrix elements of the four-body 2DVM Hamiltonian operators in this basis.

For nonrigid molecules, it is expected that low energy eigenstates would be better defined within the displaced oscillator basis set –$SO(3)$ dynamical symmetry– whereas states with energies above the potential barrier should be better characterized in the cylindrical oscillator basis set –$U(2)$ dynamical symmetry. Therefore, depending on the energy, vibrational bending overtones could be assigned either to symmetric top quantum labels, $\nu_b$ and $K$, or to the 2D harmonic oscillator quantum labels, $n$ and $\ell$, used in the linear case. These two sets of quantum numbers are linked by the transformation $\nu_b = \frac{n-|\ell|}{2}$ and $K = \ell$ (see, e.g. [1,15]).

### 2.2. The 2DVM Hamiltonian

In this work we make use of three different Hamiltonian operators of increasing complexity. The simplest one, $\hat{\mathcal{H}}$, has been chiefly used in the study of ground and excited state QPTs in the 2DVM. It is a very simplified Hamiltonian that includes the $\hat{n}$ operator, from

the cylindrical oscillator dynamical symmetry, and the Pairing operator $\hat{P}$, from the displaced oscillator dynamical symmetry,

$$\hat{\mathcal{H}} = \varepsilon\left[(1-\xi)\hat{n} + \frac{\xi}{N-1}\hat{P}\right]. \tag{7}$$

The number operator, $\hat{n}$, is the total number of $\tau$ bosons and has a direct physical interpretation in the cylindrical oscillator dynamical symmetry as the number of quanta of excitation in the linear limit. In fact, it is defined as $\hat{n} = \hat{n}_x + \hat{n}_y$ for a two-dimensional harmonic oscillator. The Pairing operator interpretation is not so direct, it is defined as $\hat{P} = N(N+1) - \hat{W}^2$, where the first contribution is constant and it is used for convenience to make the ground state lie at zero energy. The second term, $\hat{W}^2$, is the Casimir operator of the $SO(3)$ subalgebra. Therefore it is a squared angular momentum which, nevertheless, should not be mistaken with the physical angular momentum, that is the vibrational angular momentum, $\hat{\ell}$. The spectrum of the Pairing operator is anharmonic, its associated potential has a minimum outside the origin -thus the displaced oscillator name for the dynamical symmetry- and the number of quanta of excitation, $\nu_b$, can be obtained from the quantum number $\omega$ as shown in Eq. (6). The interested reader can find more details in Ref[7].

The Hamiltonian (7) has two parameters: a global energy scale $\varepsilon$ and a control parameter $\xi$. For $\xi = 0.0$, the system is in the first dynamical symmetry (linear limit) while for $\xi = 1.0$ the system is in the second one (bent limit). The different values of the control parameter $\xi \in [0, 1]$ quantifies the weight of one limit or the other. This is specially adequate in the characterization of ground and excited state QPTs. A second-order ground state QPT occurs for the critical value $\xi_c = 0.2$ [7]. In the present work we use this simplified model Hamiltonian to illustrate the use of the participation ratio as an ESQPT probe. In order to perform fits to observed bending spectra, the Hamiltonian should include more interactions.

It is very illustrative to compute the quasilinearity parameter, $\gamma_0$, introduced by Yamada and Winnewisser [1,86] computed from the spectrum of Hamiltonian (7) for different values of the $\xi$ control parameter. The $\gamma_0$ parameter is defined as the ratio of two energy gaps and aims to locate a particular molecule between the semirigid linear ($\gamma_0$ = -1) and bent ($\gamma_0 = 1$) limits

$$\gamma_0 = 1 - 4\frac{E(\nu_b = 0, \ell = 1) - E(\nu_b = 0, \ell = 0)}{E(\nu_b = 1, \ell = 0) - E(\nu_b = 0, \ell = 0)}, \tag{8}$$

where in the bent and nonrigid cases the $\ell$ label is replaced by the $K$ one. In order to make a comparison between the two parameters, we have depicted in Fig. 1 a correlation diagram that shows the value of $\gamma_0$ as a function of $\xi$ for $\xi \in [0, 1]$ and different system sizes.

As expected, the $\gamma_0$ value varies from -1 for $\xi = 0$ to 1 for $\xi = 1$ displaying a sudden change around the critical value of the control parameter, $\xi_c = 0.2$, where the system spectroscopic features change from linear to bent through a nonrigid configuration [6,7]. This change becomes more abrupt the larger the system size, something that is explained by the fact that the true shape phase transition happens in the mean field limit, i.e. for large $N$ values. In fact, the quasilinearity parameter (8) would be a possible order parameter to characterize the ground state quantum phase transition in the 2DVM. The finite-size scaling properties of this transition were studied analitically in [36].

A second Hamiltonian of interest is $\hat{H}_{2b}$, the most general one- and two-body Hamiltonian of the 2DVM [7,28]

$$\hat{H}_{2b} = E_0 + \epsilon\hat{n} + \alpha\hat{n}(\hat{n}+1) + \beta\hat{\ell}^2 + A\hat{P}. \tag{9}$$

The operators $\hat{n}$ and $\hat{n}(\hat{n}+1)$ are the first and second order Casimir operators of $U(2)$ algebra in the cylindrical oscillator chain. Therefore, the operator $\hat{n}(\hat{n}+1)$ is an anharmonic correction to the linear limit bending vibration. The pairing operator $\hat{P}$, as mentioned above, is the Casimir operator of $SO(3)$ in the displaced oscillator chain, whose spectrum can be mapped to a two-dimensional anharmonic oscillator. The vibrational angular momentum, $\hat{\ell}$, is common to both dynamical symmetries and it is the physical angular momentum of the two-dimensional system. In fact, in all the cases considered, the angular momentum is a constant of the motion, $\ell$ is a good quantum number, and the Hamiltonian matrix is block diagonal in $\ell$. This fact simplifies numerical calculations, reducing matrix dimensions. This reduction is further increased because for $\ell \neq 0$ only positive angular momentum values are considered. This is explained because, in absence of symmetry-breaking external fields, the first order angular momentum operator $\hat{\ell}$ is not included in the Hamiltonian and there positive and negative $\ell$ value levels are degenerate.

The third Hamiltonian considered is $\hat{H}_{4b}$, the most general 1-, 2-, 3-, and 4-body Hamiltonian expressed as follows

$$\begin{aligned}\hat{H}_{4b} =& P_{11}\hat{n} \\ &+ P_{21}\hat{n}^2 + P_{22}\hat{\ell}^2 + P_{23}\hat{W}^2 \\ &+ P_{31}\hat{n}^3 + P_{32}\hat{n}\hat{\ell}^2 + P_{33}(\hat{n}\hat{W}^2 + \hat{W}^2\hat{n}) \\ &+ P_{41}\hat{n}^4 + P_{42}\hat{n}^2\hat{\ell}^2 + P_{43}\hat{\ell}^4 + P_{44}\hat{\ell}^2\hat{W}^2 \\ &+ P_{45}(\hat{n}^2\hat{W}^2 + \hat{W}^2\hat{n}^2) + P_{46}\hat{W}^4 + P_{47}(\hat{W}^2\hat{\bar{W}}^2 + \hat{\bar{W}}^2\hat{W}^2)/2.\end{aligned} \tag{10}$$

This Hamiltonian has fourteen spectroscopic constants $P_{ij}$, where the subindexes indicate that the parameter is the $j$-th operator among the $i$-body interactions. The operators have been conveniently symmetrized when they involve products of non-commuting operators. The physical interpretation of the role of the three- and four-body operators in this Hamiltonian is still quite clear: $\hat{n}^3$ and $\hat{n}^4$ are further anharmonic resonances in the linear limit; $\hat{\ell}^4$ is a centrifugal correction; and $\hat{W}^4$ is an anharmonic correction to the displaced oscillator (bent limit). The operators $\hat{n}\hat{\ell}^2$ and $\hat{n}^2\hat{\ell}^2$ are vibration rotational terms in the linear limit, as well as $\ell^2\hat{W}^2$ for the bent limit. The resonances $\hat{n}\hat{W}^2 + \hat{W}^2\hat{n}$ and $\hat{n}^2\hat{W}^2 + \hat{W}^2\hat{n}^2$ mix the two limits of the model. Finally, the term $\hat{W}^2\hat{\bar{W}}^2 + \hat{\bar{W}}^2\hat{W}^2$ is a resonance that involves the Casimir operators for the $SO(3)$ and $\overline{SO(3)}$ subalgebras in the model, associated with two possible realizations for the displaced oscillator chain [7]. This last parameter has only been included for completeness as it has not been found necessary in any of the fits for the different molecules considered in this work. The same happens for the $\hat{n}^3$ and $\hat{n}^4$ operators.

From the matrix elements of the creation and annihilation $\sigma$ and $\tau$ bosons in the two bases associated with the model dynamical symmetries, published in [7], the operator matrix elements of all operators in Eq. (10) can be derived. We provide the matrix elements of the operators in the two bases of interest as an appendix to the present work.

### 2.3. ESQPT and participation ratio

It has been recently shown that in all vibron model limits the ESQPT occurring between the $U(N-1)$ and $SO(N)$ dynamical symmetries (for $N = 2, 3, 4$) implies a strong localization of the wave function for the state(s) closer to the critical energy of the transition when expressed in the $U(N-1)$ basis. This fact has important consequences in the system dynamics [73,87,88]. A convenient quantity to reveal this localization is the PR [59]. This quantity, closely linked to the Shannon entropy [89], is also named inverse participation ratio [90] or number of principal components [89]. If we consider a basis $\{|\psi_i\rangle\}_{i=1}^{dim}$, we can express the eigenstates of our problem as $|\Psi_k\rangle = \sum_{i=1}^{dim} c_{ki}|\psi_i\rangle$, with the usual normalization $\sum_{i=1}^{dim} c_{ki}c^*_{k'i} = \delta_{k'k}$. The PR is defined as the inverse of the sum of

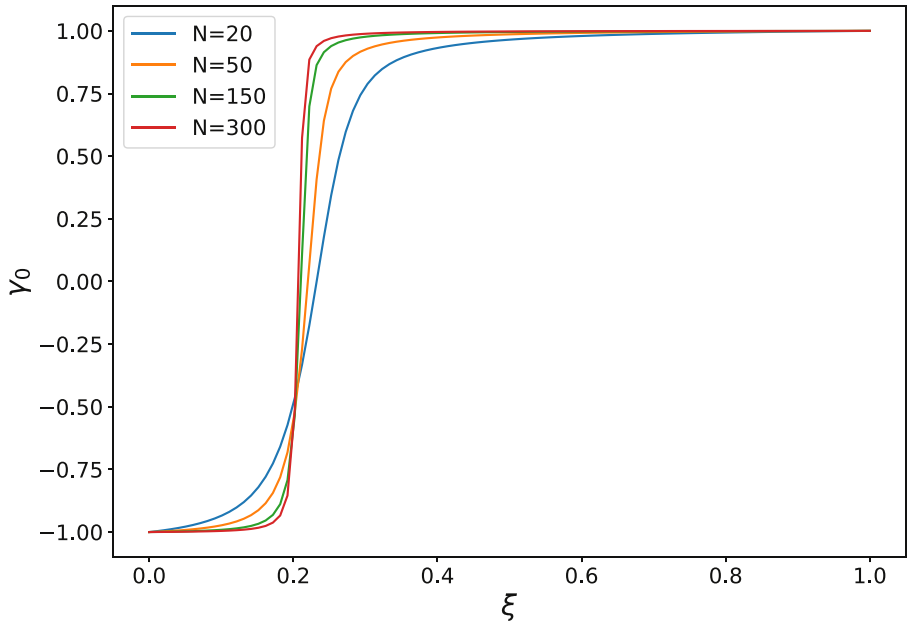


**Fig. 1.** Quasilinearity parameter $\gamma_0$ [86] given in Eq. (8) evaluated from the spectrum obtained with model Hamiltonian (7) for control parameter values $\xi \in [0, 1]$ and different $N$ values.

$c_{ki}c^*_{ki}$ squared:

$$PR[\Psi_k] = \frac{1}{\sum_{i=1}^{dim} |c_{ki}|^4}. \tag{11}$$

The minimum value of the PR for a given state is one, when the eigenfunction corresponds exactly with a basis state and all $c_{ki}$ components are zero besides one which is equal to unity. This entails a maximum localization in the selected basis. On the other hand, the maximum value of the PR is *dim*, the dimension of the Hamiltonian block. This value is attained once the wavefunction has all their components equal and non-zero. In the present case we can express the eigenstates in one of the two bases associated with the $U(3)$ dynamical symmetries,

$$|\Psi_k^{(\ell)}\rangle \begin{cases} \nearrow \; |\Psi_k^{(\ell)}\rangle = \sum_n c_{kn}^{(\ell)} |[N]; n^\ell\rangle \quad \text{(Cylindrical oscillator chain)} \\ \searrow \; |\Psi_k^{(\ell)}\rangle = \sum_{v_b} d_{kv_b}^{(\ell)} |[N]; v_b \ell\rangle \quad \text{(Displaced oscillator chain).} \end{cases} \tag{12}$$

PR values are usually normalized, dividing the value obtained from Eq. (12) by the dimension of the space. This facilitates comparing results for systems with different sizes. The results obtained for the model Hamiltonian (7) help to illustrate the information provided by the PR quantity. The ground state QPT for the model Hamiltonian happens for the critical control parameter value $\xi_c = 0.2$ and the ESQPT occurs for control parameters values larger than $\xi_c$. The ESQPT is marked by a nonanaliticity of the energy level density at the critical energy in the thermodynamic or mean field limit ($N \to \infty$). This critical point can be reached in two different ways: *(i)* varying a Hamiltonian control parameter, within a certain range, for a constant excitation energy; or *(ii)* increasing the excitation energy for a Hamiltonian with constant parameters. In Fig. 2 we depict the correlation energy diagram for $N = 2000$ and $0 \le \xi \le 1$ and we plot the PR for the cylindrical (left panel) and displaced (right panel) oscillator basis as a heat map. The left panel shows the high localization of the states on the separatrix that marks the ESQPT (low PR values) when expressed in the cylindrical oscillator basis. States located above the separatrix have a $U(2)$ character –being closer to a linear configuration– while states below the separatrix have a $SO(3)$ character – and are closer to a bent configuration. For a high enough barrier to linearity, states with a bent character are more localized in the $SO(3)$ basis and states closer to a linear configuration are better localized in the $U(2)$ basis, respectively. Thus, under the barrier, PR values in the $SO(3)$ basis are less than PR values in the $U(2)$ basis. This pattern reverses as energy crosses the barrier to linearity. However, if the barrier to linearity is low, and therefore the system lies far from any dynamical symmetry, there is a substantial mixing in both bases and it may happen that, under the barrier, the PR in the $U(2)$ basis is similar or less than the PR in the $SO(3)$ basis. Therefore, in cases far from the dynamical symmetries the PR is a probe too coarse to assign $U(2)$ or $SO(3)$ character to a state. In spite of this, as illustrated in the left panel of Fig. 2, the minimum of the PR value in the $U(2)$ basis always allows for a precise determination of the critical energy of the ESQPT.

### 2.4. Mean field limit of the 2DVM

The zero temperature ground and excited state QPTs truly occur in the thermodynamic limit –or mean field limit– of the system, for large system sizes (large $N$ values). In any case, the derivation of a classical energy functional from the algebraic Hamiltonian is of great help in understanding and classifying these phenomena. A classical energy functional, within a $1/N$ approximation, can be obtained using the coherent or intrinsic state formalism. This formalism, originally introduced by Gilmore [31], was applied in the first instance to algebraic models in nuclear physics [60], and it was later extended to molecular systems [61]. We present here the basic results, further details about the intrinsic state formalism results for the 2DVM model can be found in Ref. [7].

The initial step is the consideration of the coherent (or intrinsic) ground state

$$|[N]; \mathbf{r}\rangle = \frac{1}{\sqrt{N!}} \left(b_c^\dagger\right)^N |0\rangle, \tag{13}$$

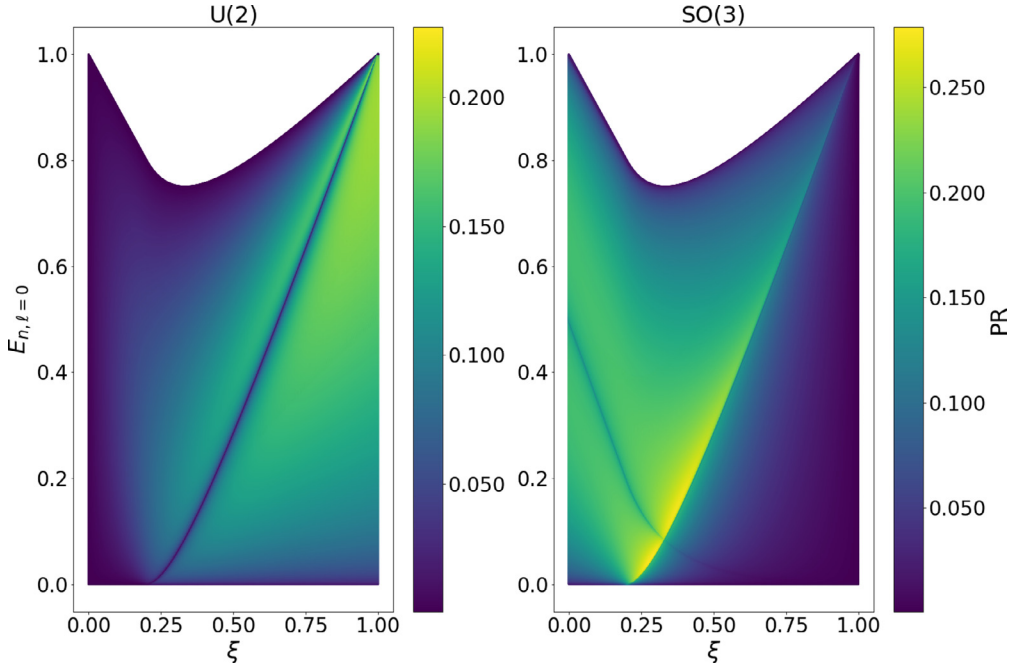


**Fig. 2.** Both panels represent the normalized excitation energies for $\ell = 0$ states with $N = 2000$ versus the $\xi$ parameter of the model Hamiltonian (7). Each energy point is colored in accordance with the value of the normalized PR for the corresponding eigenstate expressed in the cylindrical oscillator (left panel) or the displaced oscillator (right panel) basis.

that is normalized, and where $\mathbf{r}$ stands for the 2D classical coordinates and $b_c^\dagger$ is the boson condensate operator

$$b_c^\dagger = \frac{1}{\sqrt{1+r^2}}\left[\sigma^\dagger + x\tau_x^\dagger + y\tau_y^\dagger\right]. \tag{14}$$

Calculating the expectation value of the Hamiltonian (10) in the coherent state (13) we obtain the system energy functional $E(r)$

$$E(r) = \langle [N]; \mathbf{r}|\hat{H}_{4b}|[N]; \mathbf{r}\rangle \tag{15}$$

The results for the different terms composing the four-body algebraic Hamiltonian (10) can be found in Appendix B.

The one- and two-body Hamiltonian phase diagram was studied in [7] and it implies a single control parameter and a second order ground state phase transition between the linear and bent limits, as expected [30]. The role of the anharmonicity was studied in [72]. The inclusion of three- and four-body operators in Hamiltonian implies a significantly more complex phase diagram and we are currently working in its characterization. Once this task is accomplished we will have a number of essential control parameters, $\xi_1, \xi_2, \ldots$ and the correlation between them and the quasilinear parameter (8) can be worked out.

The complete classical limit of the system is obtained considering a complex variational parameter in the boson condensate (14). The real and imaginary parts of the variable are mapped to coordinate and momenta of the system. We perform a simpler transformation, with a real $r$ parameter to obtain the system energy functional. The comparison of this energy functional to the bending potentials used in configuration space is far from direct. As mentioned above, the coherent approximation is valid only up to a $1/N$-order. Considering the $N$ values involved in the study of molecular benders this is a significant uncertainty. It is possible to go beyond the mean field limit [36], but before embarking in this procedure one should grapple with two other issues that also hinder the above mentioned comparison. The first one is that the kinetic energy obtained in the intrinsic state approach is position-dependent [61] and, therefore, it is not equivalent to the usual kinetic energy operator. Furthermore, one has to deal with the transformation from the dimensionless variable $r$ to a physical coordinate measuring the deviation of linearity angle, $\theta$, which implies a connection between the physical system and its algebraic realization. A linear approximation to this problem has been previously worked out for the two dynamical symmetries and extended to situations in-between [6,8]. In the present case, the use of higher-order terms in the Hamiltonian further complicates this connection. In spite of these drawbacks, and notwithstanding that the results obtained should in principle be considered of a qualitative nature, the energy functionals resulting from the coherent state approach provide a fairly intuitive grasp into the model results that helps to overcome its abstract character. Therefore, in the nonrigid molecules studied, we provide the resulting energy functionals to help in the interpretation of the obtained results.

## 3. Results

The main advantage of the 2DVM is the possibility to encompass, in a computationally simple approach, the full gamut of behaviors expected for molecular bending vibrations: linear or bent semi-rigid configurations and the nonrigid case. The latter one is characterized by a large amplitude, highly anharmonic, degree of freedom and its modeling is only achieved using a Hamiltonian operator that combines interactions from the linear and bent dynamical symmetries.

In order to bring to light the 2DVM versatility, we model bending vibrational data for four molecules which have very different spectroscopic signatures: one semirigid linear (HNC), one semirigid bent ($H_2S$), and two nonrigid molecules ($Si_2C$ and NCNCS) with a large amplitude bent-to-linear mode. In all cases, the bending spectrum has been reproduced making use of the most general 4-body Hamiltonian (10). For this purpose, we have collected the available data for the bending degree of freedom under study. The 2DVM model only deals with vibrational bending levels, therefore it is necessary that the experimental ro-vibrational term values are fitted and assigned making use of a model able to extract the vibrational origins from the rotational spectra for each vibrational band. This vibrational origins are the data we used as a reference

**Table 1**
Optimized Hamiltonian parameters ($P_{ij}$, in $cm^{-1}$ units) for the selected bending degree of freedom of HNC, $H_2S$, $Si_2C$, and NCNCS. Values are given with their associated uncertainty (one $\sigma$ confidence interval) between parentheses in units of the last quoted digits. The total vibron number, $N$, the *rms* obtained in the fit (in $cm^{-1}$ units), and the number of data entering the minimization algorithm, $N_{data}$, are also included.

| Molecule | HNC | $H_2S$[a] | $Si_2C$ | NCNCS |
|---|---|---|---|---|
| $P_{11}$ | 1414.0(4) | - | 63.8(5) | 331.97(8) |
| $P_{21}$ | −29.837(15) | - | −0.108(18) | −2.0954(6) |
| $P_{22}$ | 15.81(10) | 2.897(13) | 0.98(5) | 1.190(8) |
| $P_{23}$ | −8.054(3) | −3.0113(12) | −0.8117(17) | −0.58578(17) |
| $P_{32}$ | $4.9(10)\times10^{-2}$ | - | - | - |
| $P_{42}$ | - | - | - | $-2.65(20)\times10^{-5}$ |
| $P_{43}$ | - | $-5.7(3)\times10^{-5}$ | - | - |
| $P_{44}$ | - | $1.235(9)\times10^{-4}$ | - | - |
| $P_{46}$ | - | $1.924(4)\times10^{-5}$ | - | $3.48(8)\times10^{-7}$ |
| $N$ | 40 | 121 | 49 | 150 |
| *rms* | 0.08 | 0.20 | 1.48 | 0.79 |
| $N_{data}$ | 19 | 96 | 37 | 88 |

[a] Two additional parameters besides those listed in this table are used in this case to account for rotational effects. See Subsection 3.2.

for our model, though in the $H_2S$ case (see Subsection 3.2) we include in our calculation the effect of the rotational structure in order to optimize the agreement with the reported energy values.

Making use of this information, the $P_{ij}$ spectroscopic parameters of Hamiltonian (10) have been optimized to reproduce the reported bending spectra, obtaining in all cases a good agreement between our results and reported data. We have developed a Fortran source code for the calculation of the algebraic Hamiltonian (10) eigenvalues and eigenstates, as well as the different quantities included in the present work. The code makes use of the LAPACK [91] and LAPACK95 [92] libraries for matrix diagonalization and it also performs the requested state assignment tasks. The parameter optimization procedure is a nonlinear least square fitting using the *Minuit* Fortran code [93]. In every molecule we start from the two-body minimal Hamiltonian (9), fixing to zero the three- and four-body operators. This Hamiltonian has been previously used in the modeling of three out of the four cases under study [8,56]. After that, the effects of different combinations of three- and four-body parameters are studied, including them in the minimization and using the statistical information provided by Minuit to choose a minimal set of physically relevant parameter. The minimization finishes once convergence is reached for a set of parameters and a careful check of the obtained results has been carried out, to ascertain their physical character. As can be seen in Tab. 1, not all possible $P_{ij}$ parameters in the general algebraic Hamiltonian (10) have been used. The code is available under request to the authors and it will be published in a forthcoming work.

Apart from the $P_{ij}$ spectroscopic parameters, there is an extra parameter, the total number of bosons $N$. The integer nature of this quantum number hinders its inclusion in the *Minuit* minimization. Instead, following the methods published in the appendix of [8], we have manually adjusted it to optimize the agreement with reported data. In the HNC, NCNCS, and $H_2S$ we have used as initial $N$ values those reported in [8,56]. In a recent work, it has been possible to estimate a lower bound for the N parameter in isomerizing systems [71].

The agreement between calculated ($\{E_k^{calc}\}_{k=1}^{N_{data}}$) and reported results ($\{E_k^{ref}\}_{k=1}^{N_{data}}$) is assessed using the *rms*, defined as follows

$$rms = \sqrt{\frac{\sum_{k=1}^{N_{data}} \left(E_k^{calc} - E_k^{ref}\right)^2}{N_{data} - n_p}}, \tag{16}$$

where $n_p$ is the number of free parameters in the optimization routine.

To facilitate the comparison between the different cases, we report in Tab. 1 the optimized parameters in the four cases studied as well as their one $\sigma$ confidence interval. As mentioned above, not all possible $P_{ij}$ parameters in the general algebraic Hamiltonian (10) have been used. We have organized this section into four subsections, where we discuss the results obtained for each molecule. We also include in this table the value of the total number of bosons, $N$, the *rms* of the fit, and the number of vibrational levels involved in the minimization process.

As mentioned above, the present work can be considered as an extension of previous works where most fits were performed with a two-body Hamiltonian [8,56]. We have reviewed the results previously obtained making use of the four-body 2DVM Hamiltonian (10) and the agreement in some cases have notably improved with the addition of operators of three- or four-body character, e.g. the HNC case with an *rms* that has decreased from 2.3 to 0.08 $cm^{-1}$ with the addition of a single three-body operator.

Apart from the calculation of the fit to the spectrum, we have tried to cast some light upon the dynamical structure of the different molecular systems. We show in the four cases under study their quantum monodromy diagram, Birge-Sponer plot, and participation ratio plot. The quantum monodromy diagrams and the Birge-Sponer plots include experimental and calculated bending energy values, as well as the algebraic four-body Hamiltonian model predictions for yet unknown energy levels. The PR plots include the results for the optimized zero vibrational angular momentum eigenstates expressed in the cylindrical (2) and displaced oscillator (4) bases versus the state energy. In the two nonrigid cases, we include as insets in the PR panel the classical energy functional obtained with the coherent state approach to offer a more intuitive view of the 2DVM results. Tables with the values of predicted levels and a residuals plot can be found in the Supplementary Material.

### 3.1. Hydrogen isocyanide, HNC

Hydrogen isocyanide is an isomer of hydrogen cyanide and a linear molecule. From the many experimental ro-vibrational term values in the literature, we have selected the 19 available pure $\nu_2$ experimental energy levels [94]. In the case of linear and quasilinear molecules, the interactions included in the cylindrical oscillator subalgebra chain (1) are the most relevant, although once the molecule starts departing from a rigidly-linear behavior, interactions like $\hat{W}^2$, attached to the displaced oscillator chain in Eq. (1), are also required. This is specially true for quasilinear molecules, due to the flatness of the potential that characterizes systems close to the ground state QPT [8,56].

We have obtained a sizable improvement in the fit to this molecule with respect to the results published in Ref. [56]; managing to get a decrease in the *rms* from 2.3 $cm^{-1}$ to 0.08 $cm^{-1}$ with

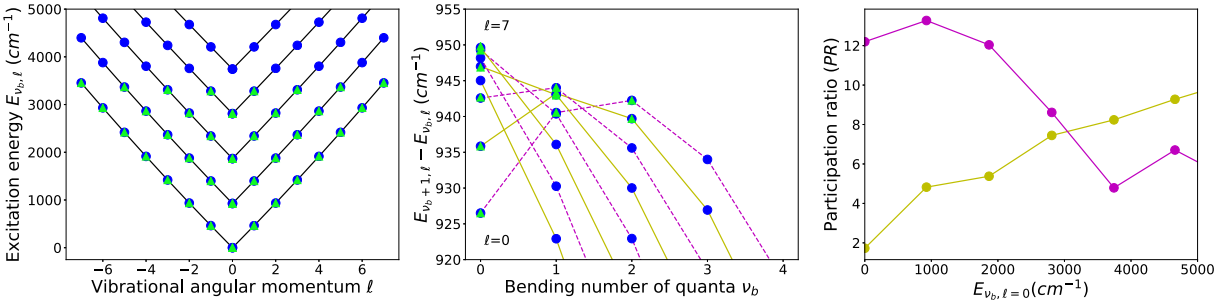


**Fig. 3.** $\nu_2$ bending mode of HNC. Left panel: Quantum monodromy plot. Central panel: Birge-Sponer plot. In the left and central panels blue circles (green triangles) are calculated (experimental) data. Right panel: Participation Ratio of $\ell = 0$ eigenstates in the $U(2)$ (yellow line) and $SO(3)$ (magenta line) bases as a function of the state energy. (For interpretation of the references to colour in this figure legend, the reader is referred to the web version of this article.)

**Table 2**
Experimental and calculated term values and residuals for the bending mode of HNC. Units of $cm^{-1}$.

| $(n, \ell)$[a] | Exp.[b] | Cal.[c] | Exp.-Cal.[d] |
|---|---|---|---|
| (2 0) | 926.50 | 926.5071 | −0.007 |
| (4 0) | 1867.05 | 1867.0497 | 0.000 |
| (6 0) | 2809.29 | 2809.2992 | −0.009 |
| (1 1) | 462.72 | 462.6863 | 0.034 |
| (3 1) | 1398.56 | 1398.5296 | 0.030 |
| (5 1) | 2341.84 | 2341.7558 | 0.084 |
| (7 1) | 3281.50 | 3281.4508 | 0.049 |
| (2 2) | 936.05 | 936.1066 | −0.057 |
| (4 2) | 1878.72 | 1878.6866 | 0.033 |
| (6 2) | 2822.75 | 2822.7088 | 0.041 |
| (3 3) | 1419.97 | 1419.9198 | 0.050 |
| (5 3) | 2366.83 | 2366.9073 | −0.077 |
| (7 3) | 3309.78 | 3309.9472 | −0.167 |
| (4 4) | 1913.87 | 1913.8403 | 0.030 |
| (6 4) | 2863.11 | 2863.1206 | −0.011 |
| (5 5) | 2417.57 | 2417.6251 | −0.055 |
| (7 5) | 3367.37 | 3367.2552 | 0.115 |
| (6 6) | 2930.90 | 2931.0649 | −0.165 |
| (7 7) | 3453.78 | 3453.9760 | −0.196 |

[a] Cylindrical oscillator basis quantum labels assigned to the optimized eigenvectors.
[b] Experimental energies from Ref. [94].
[c] Calculated energies.
[d] Difference between experimental and calculated energies.

the addition of only one extra interaction: the 3-body term $\hat{n}\hat{\ell}^2$. The experimental and calculated vibrational energies are reported in Tab. 2. All the states are well below the isomerization transition state energy, which lies around 12,000 $cm^{-1}$ [71].

The calculated energies and eigenstates for the optimized Hamiltonian have been used in preparing the figures in the different panels of Fig. 3 where the quantum monodromy plot (left panel) indicates a linear equilibrium geometrical configuration for this molecule. However, the Birge-Sponer diagram (center panel of Fig. 3) is more complex than expected for a linear molecule, with noticeably different behavior for states with different vibrational angular momentum values. Besides, the participation ratio diagram (right panel of Fig. 3) shows, for $\ell = 0$ states, a crossing around 3,000 $cm^{-1}$ after which states are more localized in the $SO(3)$ basis set than in the $U(2)$ basis set. As already highlighted in Ref. [56], the Birge-Sponer plot indicates that there is a competition between anharmonicity and pairing operators in the subspaces with different vibrational angular momenta. The inclusion of the new cubic term seems to conveniently tackle with this. In any case, the eigenvectors are more complex than expected for a semirigid linear molecule, as can be deduced from the crossing of the two curves of the PR plot. This could be due to the influence of the isomerization barrier for this system. However, it lies at 12,000 $cm^{-1}$, too far to explain such a low energy feature in the PR [71]. The HNC system, as energy increases, is characterized by a large mixing of states in both bases which, as explained in Subsec. 2.3, makes the PR unable to unambiguously ascribe a linear or bent character to the wave function.

### 3.2. Hydrogen sulfide, $H_2S$

The rovibrational spectrum of hydrogen sulfide has been exhaustively studied (see, e.g., Ref. [95] and references therein). Rovibrational energies for bending overtones are known in bands up to $\nu_2 = 5$, inclusive [96–101]. This is a bent molecule and only interactions associated with the displaced oscillator dynamical symmetry have been required in order to obtain a good fit.

The $H_2S$ molecule is an asymmetric-top and its experimental $\nu_2$ bending states are therefore labeled as $|\nu_b; J, K_a, K_c\rangle$, where the quantum numbers $K_a$ and $K_c$ are the projections in the molecular fixed frame system of the rotational angular momentum $J$ along the $z$-axis (assuming the $I^r$ and $III^r$ conventions, respectively). In this case, one should start by selecting those states that are more into the 2DVM scope, taking into account that in the SO(3) dynamical symmetry, the model can be mapped into a 2D truncated rovibrator, and the $\ell$ angular momentum can be identified with $K$, the angular momentum projection on the figure axis of the molecule. Therefore, in the case of asymmetric top molecules, one should consider whether the molecule is closer to a prolate or oblate rotator. Hydrogen sulfide is closer to the oblate limit, and therefore we have used as an input for the model the 96 available experimental bending rovibrational levels $|\nu_b; J, K_a = 0, K_c = J\rangle$, with $J = K_c = 0, \ldots, 20$ with $A_1$ (even $J$) or $B_1$ (odd $J$) symmetry (for a discussion on the symmetry of these states see, for example, [95,102]).

In this case, we have added to the Hamiltonian (10) two extra operators that are linear in the absolute value of the vibrational angular momentum, $|\ell|$, associated with the spectroscopic parameters $B$ and $B_{\nu_b}$.

$$\hat{H}_{bent} = \hat{H}_{4b} + B|\ell| + B_{\nu_b}|\ell|\hat{W}^2, \tag{17}$$

These two parameters, in particular $B$, are fundamental to understand the improvement achieved in this case when comparing our results with the results in Ref. [56]. The need of these extra interaction terms in Eq. (17) can be understood considering the linear $J$ term that stems from the rotational term $J(J+1)$ in the rovibrational Hamiltonian while the operator associated with the $B_{\nu_b}$ parameter introduces an extra centrifugal correction [95,102].

Our analysis started with the fit of the Hamiltonian (10) relevant parameters, those associated with the displaced oscillator dynamical symmetry (see Tab. 1), obtaining an *rms* of 11.02 $cm^{-1}$. Once the parameter $B$ is included, the *rms* decreases to 0.93 $cm^{-1}$. The final result has an *rms* of 0.20 $cm^{-1}$. The optimized values of the $B$ and $B_{\nu_b}$ parameters are $B = 18.98(21)$ and $B_{\nu_b} = -6.29(15) \times$

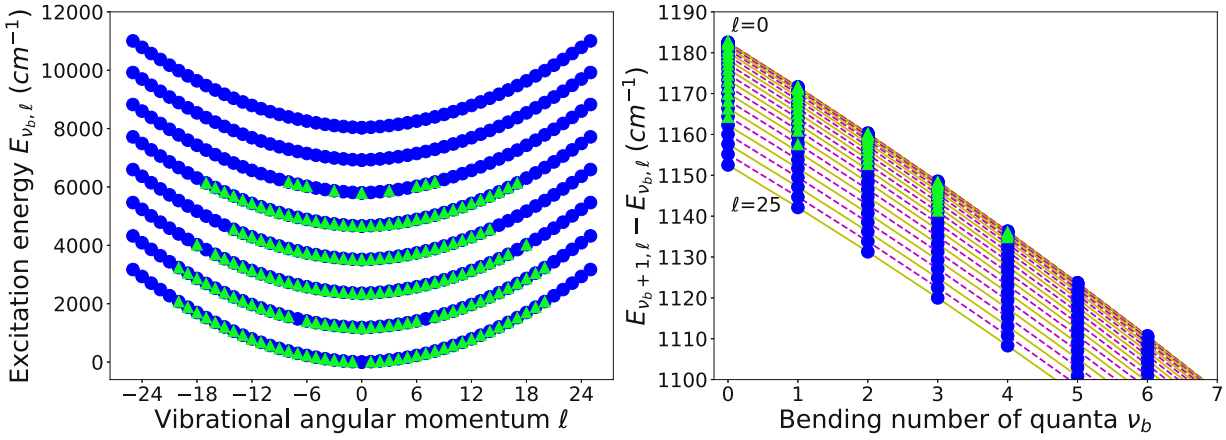


**Fig. 4.** $\nu_2$ bending mode of $H_2S$. Left panel: quantum monodromy plot. Right panel: Birge-Sponer plot. In both panels blue circles (green triangles) are calculated (experimental) data. (For interpretation of the references to colour in this figure legend, the reader is referred to the web version of this article.)

$10^{-4}$, both in $cm^{-1}$ units. The calculated bending energy levels, shown in Tab. 3, have a satisfactory agreement with the experimental data. This agreement is markedly better than the agreement obtained in Ref. [56], where only 35 experimental term values were included in the fit. Therefore, the present four-body Hamiltonian, plus the rotational energy correction, achieves a significant improvement in the optimization and, in our experience, within these accuracy levels, the predicted spectra can help in the labeling of not-yet-assigned experimental energy levels. The residual plot included in the Supplementary Material section displays clear tendencies in the calculated energy differences. To explain this, one has to take into consideration that experimental data reach large K values ($K = 20$) and the present work is a global rovibrational analysis for the bending vibration. Thus, we have systematic errors in the vibrational headbands, due to the neglect of stretch-bend interactions. In addition to this, we only include operators up to fourth order in the quantum number $K$, while, in a band by band analysis, higher order interactions are considered (e.g. see Ref. [100]).

The energy term values and eigenvectors obtained from the optimized Hamiltonian have been used to compute the quantities depicted in the two panels of Fig. 4. The quantum monodromy plot (left panel) and Birge-Sponer diagram (right panel) obtained in this case are textbook examples of a semirigid bent molecular species. As in this case all the $\hat{H}_{4b}$ operators included belong to a dynamical symmetry, we decided not to include the PR. In the $SO(3)$ basis all eigenstates have PR equal to unity and maximal localization, while in the $U(2)$ case the PR would be given by the transformation bracket between the two basis.

### 3.3. Disilicon carbide, $Si_2C$

Disilicon carbide is a floppy triatomic molecule [103–105] which, in recent years, has been the subject of a number of experimental works on its rotational and rovibrational spectra [21,106] mostly motivated by the relevance of silicon and carbon clusters in astronomy and in technical applications. The presence of this molecule in IRC + 10216 was confirmed in 2015 [107].

The large amplitude motion of $Si_2C$ stems from the $\nu_2$ bending mode. The available experimental rovibrational term values of the excited $\nu_2$ bands, up to $\nu_b = \nu_2 = 13$ and $\ell = 3$ (approx. up to 1600 $cm^{-1}$) denote a pronounced quantum monodromy effect [21]. This dataset has been used as an input to optimize the four one- and two-body spectroscopic parameters in Hamiltonian (10). They have been fitted to reproduce a total of 37 available experimental data with an *rms* of 1.48 $cm^{-1}$ (see Tab. 1). Note that this result is slightly less than the reported experimental uncertainty of 2 $cm^{-1}$ [21] and it can be considered a very good agreement with the reported data. It does not seem necessary to include higher order interactions in this case and our results can be compared to the results reported in previous works [21,108] though taking into account that these calculations are not of a phenomenological nature. In both Refs. [21,108], the rovibrational energies are obtained from an *ab initio* potential energy surface. The bending energies obtained with the present approach, labeled with displaced oscillator (bent molecule) quantum numbers, are reported in Tab. 4, together with the reported experimental data values and fit residuals.

The calculated energies and bending eigenstates have been used to compute the different quantities displayed in Fig. 5. The quantum monodromy diagram –left panel– and the Birge-Sponer plot –mid panel– are in very good accordance with the results published in Refs. [21,108], with a critical ESQPT energy and Dixon dip at $\nu_b = 6$, and a barrier to linearity that extends up to around 700 $cm^{-1}$. The PR results, depicted in the right panel, behave as expected. The PR for states up to the second overtone in the $SO(3)$ basis is under the PR expressed in the $U(2)$ basis, which implies a larger eigenstate localization for the displaced oscillator basis. The trend is reversed for higher energy values. In particular, this plot illustrates vividly the predicted localization effects in the $U(2)$ basis for the $\nu_b = 6$ overtone, the closest one to the critical ESQPT energy. As expected, the closest states to the critical energy have a very large component in the $|n = 0^{\ell=0}\rangle$ basis state [73,87,88]. For energies above the barrier, states have a linear character and the PR in the $U(2)$ basis is less than the PR in the $SO(3)$ one. The energy functional is given as a inset in the right panel of Fig. 5. From the energy functional the barrier to linearity value can be estimated to be around $\sim 675$ $cm^{-1}$. As explained in Subsec. 2.4, the implicit $1/N$ errors in the mean field approximation and the difference between the kinetic energy operators can explain why the value is too low, when compared with the values 783(48) $cm^{-1}$ -from the information of the Dixon dip [21]- and 832 $cm^{-1}$ obtained using *ab initio* calculations [108].

### 3.4. Cyanogen isothiocyanate, NCNCS

In this subsection we apply the 2DVM to the $\nu_7$ bending mode of cyanogen isothiocyanate (NCNCS), a nonrigid molecule characterized by a large amplitude CNC bending [11,109]. The spectrum for this mode has been carefully charted in the microwave and millimeter ranges for several highly-excited $\nu_7$ states and this

**Table 3**
Experimental and calculated term values and residuals for the bending mode of $H_2S$ with quantum numbers $(v_b, J, K_a = 0, K_c = J)$ ($A_1$ or $B_1$ symmetry). Units of $cm^{-1}$.

| $(v_b, K)$[a] | Exp.[b] | Cal.[c] | Exp.-Cal.[d] |
|---|---|---|---|
| (0 1) | 13.75 | 14.4158 | −0.66952 |
| (0 2) | 38.02 | 38.2719 | −0.25581 |
| (0 3) | 71.42 | 71.5662 | −0.14191 |
| (0 4) | 114.17 | 114.2953 | −0.12315 |
| (0 5) | 166.34 | 166.4546 | −0.11116 |
| (0 6) | 227.94 | 228.0378 | −0.09286 |
| (0 7) | 298.97 | 299.0375 | −0.06786 |
| (0 8) | 379.41 | 379.4448 | −0.03755 |
| (0 9) | 469.25 | 469.2497 | −0.00365 |
| (0 10) | 568.47 | 568.4406 | 0.03187 |
| (0 11) | 677.07 | 677.0046 | 0.06701 |
| (0 12) | 795.03 | 794.9274 | 0.09960 |
| (0 13) | 922.32 | 922.1934 | 0.12747 |
| (0 14) | 1058.93 | 1058.7857 | 0.14837 |
| (0 15) | 1204.85 | 1204.6860 | 0.16002 |
| (0 16) | 1360.03 | 1359.8745 | 0.15930 |
| (0 17) | 1524.48 | 1524.3303 | 0.14495 |
| (0 18) | 1698.14 | 1698.0309 | 0.11375 |
| (0 19) | 1881.02 | 1880.9526 | 0.06325 |
| (0 20) | 2073.06 | 2073.0702 | −0.00924 |
| (1 0) | 1182.58 | 1182.1654 | 0.41456 |
| (1 1) | 1196.47 | 1196.8248 | −0.35769 |
| (1 2) | 1220.87 | 1220.8053 | 0.06288 |
| (1 3) | 1254.26 | 1254.1050 | 0.15850 |
| (1 4) | 1296.86 | 1296.7204 | 0.14046 |
| (1 5) | 1348.76 | 1348.6469 | 0.10921 |
| (1 6) | 1409.96 | 1409.8782 | 0.08236 |
| (1 8) | 1560.27 | 1560.2244 | 0.04448 |
| (1 9) | 1649.35 | 1649.3203 | 0.03154 |
| (1 10) | 1747.71 | 1747.6830 | 0.02310 |
| (1 11) | 1855.32 | 1855.2998 | 0.01524 |
| (1 12) | 1972.17 | 1972.1563 | 0.00962 |
| (1 13) | 2098.24 | 2098.2370 | 0.00245 |
| (1 14) | 2233.52 | 2233.5248 | −0.00482 |
| (1 15) | 2377.99 | 2378.0016 | −0.01616 |
| (1 16) | 2531.62 | 2531.6475 | −0.03001 |
| (1 17) | 2694.39 | 2694.4416 | −0.05001 |
| (1 18) | 2866.29 | 2866.3615 | −0.07479 |
| (1 19) | 3047.28 | 3047.3834 | −0.10789 |
| (1 20) | 3237.33 | 3237.4822 | −0.14761 |
| (2 0) | 2353.96 | 2353.4272 | 0.53280 |
| (2 1) | 2368.02 | 2368.3260 | −0.31093 |
| (2 2) | 2392.57 | 2392.4289 | 0.14305 |
| (2 3) | 2425.98 | 2425.7339 | 0.24608 |
| (2 4) | 2468.45 | 2468.2375 | 0.21325 |
| (2 5) | 2520.10 | 2519.9351 | 0.16101 |
| (2 6) | 2580.93 | 2580.8204 | 0.10757 |
| (2 7) | 2650.94 | 2650.8861 | 0.05828 |
| (2 8) | 2730.14 | 2730.1233 | 0.01338 |
| (2 9) | 2818.50 | 2818.5219 | −0.02676 |
| (2 10) | 2916.01 | 2916.0702 | −0.06272 |
| (2 11) | 3022.66 | 3022.7555 | −0.09498 |
| (2 12) | 3138.44 | 3138.5634 | −0.12111 |
| (2 13) | 3263.34 | 3263.4784 | −0.14310 |
| (2 14) | 3397.32 | 3397.4835 | −0.15999 |
| (2 15) | 3540.39 | 3540.5604 | −0.17126 |
| (2 16) | 3692.51 | 3692.6893 | −0.17623 |
| (2 18) | 4023.85 | 4024.0181 | −0.16597 |
| (3 0) | 3513.79 | 3513.3476 | 0.44241 |
| (3 1) | 3528.02 | 3528.4819 | −0.46341 |
| (3 2) | 3552.76 | 3552.7051 | 0.05449 |
| (3 3) | 3586.21 | 3586.0153 | 0.19295 |
| (3 4) | 3628.58 | 3628.4090 | 0.17204 |
| (3 5) | 3680.00 | 3679.8815 | 0.11853 |
| (3 6) | 3740.49 | 3740.4267 | 0.06612 |
| (3 7) | 3810.05 | 3810.0371 | 0.01212 |
| (3 8) | 3888.67 | 3888.7039 | −0.03842 |
| (3 9) | 3976.33 | 3976.4169 | −0.08406 |
| (3 10) | 4073.04 | 4073.1646 | −0.12356 |
| (3 11) | 4178.78 | 4178.9341 | −0.15506 |
| (3 12) | 4293.53 | 4293.7111 | −0.17708 |
| (3 13) | 4417.29 | 4417.4801 | −0.18743 |
| (3 14) | 4550.04 | 4550.2241 | −0.18406 |
| (4 0) | 4661.68 | 4661.4963 | 0.18369 |
| (4 1) | 4676.10 | 4676.8620 | −0.76288 |
| (4 2) | 4701.06 | 4701.2035 | −0.14727 |
| (4 3) | 4734.58 | 4734.5187 | 0.06025 |
| (4 4) | 4776.88 | 4776.8044 | 0.08028 |
| (4 5) | 4828.12 | 4828.0557 | 0.06006 |
| (4 6) | 4888.30 | 4888.2666 | 0.03130 |
| (4 7) | 4957.43 | 4957.4295 | 0.00067 |
| (4 8) | 5035.51 | 5035.5357 | −0.02751 |
| (4 9) | 5122.53 | 5122.5750 | −0.04977 |
| (4 10) | 5218.47 | 5218.5358 | −0.06318 |
| (4 11) | 5323.34 | 5323.4052 | −0.06383 |
| (4 12) | 5437.12 | 5437.1691 | −0.04788 |
| (4 13) | 5559.80 | 5559.8117 | −0.01193 |
| (4 14) | 5691.37 | 5691.3162 | 0.04929 |
| (4 15) | 5831.81 | 5831.6642 | 0.14280 |
| (4 16) | 5981.11 | 5980.8360 | 0.27088 |
| (4 17) | 6139.26 | 6138.8106 | 0.44855 |
| (5 0) | 5797.24 | 5797.4504 | −0.21044 |
| (5 3) | 5870.73 | 5870.8214 | −0.09345 |
| (5 6) | 6024.00 | 6023.9173 | 0.07835 |
| (5 7) | 6092.74 | 6092.6406 | 0.10417 |
| (5 8) | 6170.33 | 6170.1960 | 0.13321 |

[a] Displaced oscillator basis quantum labels assigned to the optimized eigenvectors.
[b] Experimental energies from [96–101].
[c] Calculated energies.
[d] Difference between experimental and calculated energies.

**Table 4**
Experimental and calculated term values and residuals for the bending mode of $Si_2C$. Units of $cm^{-1}$.

| $(v_b, K)$[a] | Exp.[b] | Cal.[c] | Exp.-Cal.[d] |
|---|---|---|---|
| (1 0) | 140.0 | 141.5931 | −1.593 |
| (1 1) | 142.0 | 143.8421 | −1.842 |
| (2 0) | 273.0 | 274.6069 | −1.607 |
| (2 1) | 278.0 | 277.1851 | 0.815 |
| (3 0) | 399.0 | 398.3725 | 0.627 |
| (3 1) | 401.0 | 401.4841 | −0.484 |
| (3 3) | 425.0 | 425.7597 | −0.760 |
| (4 0) | 515.0 | 511.7915 | 3.209 |
| (4 1) | 516.0 | 515.9391 | 0.061 |
| (4 3) | 544.0 | 546.6778 | −2.678 |
| (5 0) | 613.0 | 612.6117 | 0.388 |
| (5 1) | 622.0 | 619.6988 | 2.301 |
| (5 2) | 636.0 | 637.0290 | −1.029 |
| (5 3) | 663.0 | 661.9059 | 1.094 |
| (6 0) | 695.0 | 696.4984 | −1.498 |
| (6 1) | 716.0 | 714.2134 | 1.787 |
| (6 2) | 741.0 | 741.3982 | −0.398 |
| (6 3) | 775.0 | 774.8380 | 0.162 |
| (7 0) | 770.0 | 771.9460 | −1.946 |
| (7 1) | 809.0 | 808.0725 | 0.928 |
| (7 2) | 848.0 | 847.2296 | 0.770 |
| (7 3) | 890.0 | 890.0296 | −0.030 |
| (8 0) | 861.0 | 862.3533 | −1.353 |
| (8 1) | 912.0 | 910.8638 | 1.136 |
| (8 2) | 959.0 | 959.9006 | −0.901 |
| (8 3) | 1011.0 | 1011.0350 | −0.035 |
| (9 0) | 970.0 | 968.8106 | 1.189 |
| (9 1) | 1025.0 | 1024.8626 | 0.137 |
| (9 2) | 1080.0 | 1081.3839 | −1.384 |
| (9 3) | 1140.0 | 1139.4754 | 0.525 |
| (10 0) | 1085.0 | 1087.2974 | -2.297 |
| (10 1) | 1151.0 | 1149.1694 | 1.831 |
| (10 3) | 1278.0 | 1275.7166 | 2.283 |
| (11 0) | 1214.0 | 1215.9113 | −1.911 |
| (11 1) | 1283.0 | 1282.7567 | 0.243 |
| (12 1) | 1425.0 | 1424.8196 | 0.180 |
| (13 1) | 1574.0 | 1574.7200 | −0.720 |

[a] Displaced oscillator basis quantum labels assigned to the optimized eigenvectors.
[b] Experimental energies from [21].
[c] Calculated energies.
[d] Difference between experimental and computed energies.

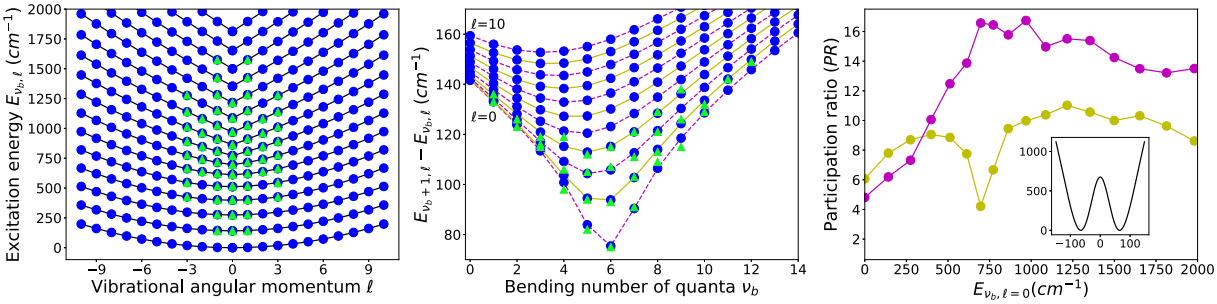


**Fig. 5.** $\nu_2$ bending mode of $Si_2C$. Left panel: quantum monodromy plot. Central panel: Birge-Sponer plot. In both panels blue circles (green triangles) are calculated (experimental) data. Right panel: Participation Ratio of $\ell = 0$ eigenstates in the $U(2)$ (yellow line) and $SO(3)$ (magenta line) bases as a function of the state energy. The bending energy functional derived using the coherent state formalism is included as an inset in the right panel. (For interpretation of the references to colour in this figure legend, the reader is referred to the web version of this article.)

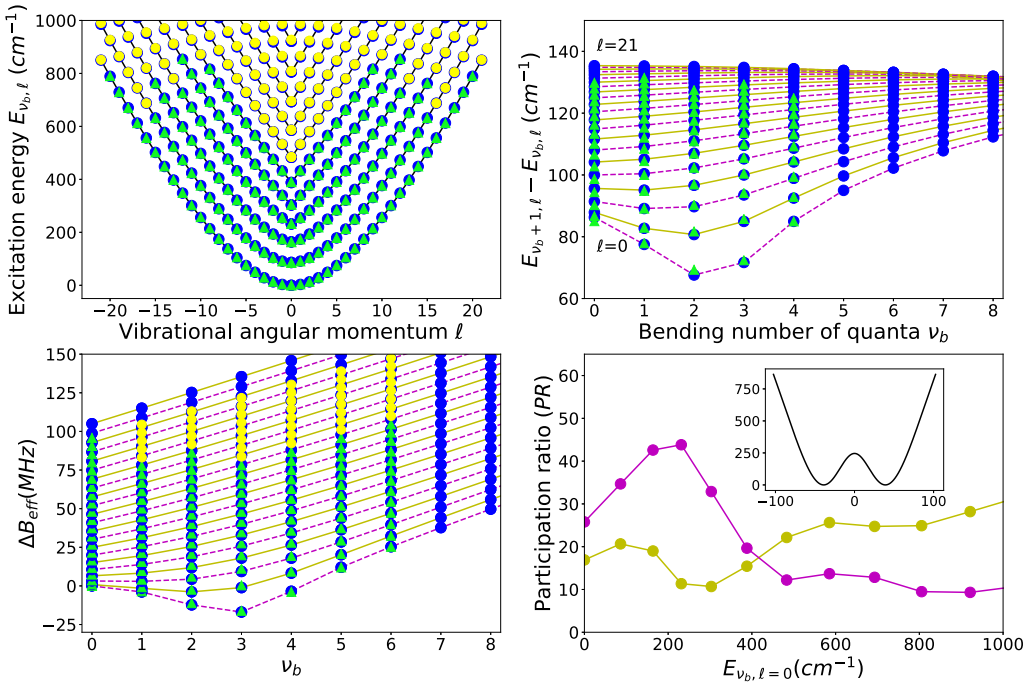


**Fig. 6.** $\nu_7$ bending mode of NCNCS. Upper left panel: quantum monodromy plot. Upper right panel: Birge-Sponer plot for the $\nu_7$ bending mode of NCNCS. Lower left panel: $\Delta B_{eff}$ for as a function of the bending excitation $\nu_b$. In these three panels blue circles (green triangles) are calculated (experimental) data. Yellow circles are predictions from [19]. Lower right panel: PR for $\ell = 0$ eigenstates in the $U(2)$ (yellow line) and $SO(3)$ (magenta line) bases as a function of the state energy. The bending energy functional derived using the coherent state formalism is included as an inset in this panel. (For interpretation of the references to colour in this figure legend, the reader is referred to the web version of this article.)

molecule has been subject of several works aiming to study quantum monodromy effects, making it one of the best examples of quantum monodromy found to date [15,17,19,20].

Being so rich in spectroscopic features, the disentangling of the spectra of NCNCS is a cumbersome task, and it displays unusual features in its rotational and vibrational spectra. In the case of Ref. [19] the GSRB model is used to allow the simultaneous treatment of rotations and vibrations and the calculation of the vibrational band origins. We use these values as an input to our model. The simultaneous treatment of rotations and vibrations is possible in the $U(4)$ based original vibron model [110], though at the cost of a more complex mathematical apparatus than the 2DVM one. However, it is possible to carry out a simpler description of the rotational spectra for nonrigid molecules within the 2DVM. In this case the $\Delta B_{eff}$ parameter, defined as $\Delta B_{eff} = B(\nu_b, \ell) - B(0, 0)$, that quantifies the rotational constant dependence on the bending number of quanta and the vibrational angular momentum -or $K$ value, $\ell = K$- can be expressed as a series expansion in the number operator [8]

$$\Delta B_{eff} = a_1 \hat{n} + a_2 \hat{n}(\hat{n}+1) + \ldots, \tag{18}$$

with $a_1 >> a_2 >> \ldots$.

In this work we analyze the CNC bending mode band origins up to $\nu_b = \nu_7 = 5$ and $K_a = 20$ reported in [19]. These data correspond to $\nu_b, J = K_a, K_a$ levels and were obtained analyzing the experimental rovibrational term values with use of the GSRB model (See Tables 8 to 11 in Ref. [19]). Eighty-eight reported band origins have been fitted using six operators of the four-body Hamiltonian (10) (full one- and two-body plus two four-body operators), with a final *rms*=0.79 $cm^{-1}$ (see Tab. 1), which improves the *rms* of 2.2 $cm^{-1}$ obtained in [8] though a direct comparison is not easy as in this paper data from [17] were used in the fit. The improvement achieved can be explained from the inclusion of the four-body interactions $\hat{\ell}^2\hat{n}^2$ and $\hat{W}^4$.

The reported and our calculated bending energies are included in Tab. 5. The residuals plot for this fit included in the Supplementary Material section displays systematic trends in each vibrational

**Table 5**
Bending band origins and calculated energy term values and residuals for the $\nu_7$ bending mode of NCNCS. Units of $cm^{-1}$.

| $(v_b, K)$[a] | $E_{origin}$[b] | Cal.[c] | $E_{origin}$-Cal.[d] | $(v_b, K)$[a] | $E_{origin}$[b] | Cal.[c] | $E_{origin}$-Cal.[d] |
|---|---|---|---|---|---|---|---|
| (0 1) | 3.42 | 3.3158 | 0.102 | (2 8) | 404.23 | 405.0085 | −0.776 |
| (0 2) | 13.38 | 13.0153 | 0.362 | (2 9) | 449.63 | 450.4394 | −0.811 |
| (0 3) | 29.24 | 28.5486 | 0.694 | (2 10) | 497.20 | 498.0187 | −0.816 |
| (0 4) | 50.32 | 49.2975 | 1.025 | (2 11) | 546.79 | 547.5617 | −0.768 |
| (0 5) | 75.99 | 74.6863 | 1.301 | (2 12) | 598.26 | 598.9047 | −0.640 |
| (0 6) | 105.70 | 104.2139 | 1.491 | (2 13) | 651.50 | 651.8997 | −0.401 |
| (0 7) | 139.03 | 137.4520 | 1.583 | (2 14) | 706.39 | 706.4114 | −0.022 |
| (0 8) | 175.61 | 174.0355 | 1.572 | (2 15) | 762.85 | 762.3142 | 0.532 |
| (0 9) | 215.11 | 213.6505 | 1.464 | (3 0) | 232.26 | 231.4167 | 0.842 |
| (0 10) | 257.30 | 256.0247 | 1.272 | (3 1) | 254.74 | 254.6472 | 0.089 |
| (0 11) | 301.93 | 300.9194 | 1.015 | (3 2) | 283.01 | 283.2800 | −0.267 |
| (0 12) | 348.84 | 348.1224 | 0.716 | (3 3) | 315.44 | 315.9345 | −0.493 |
| (0 13) | 397.84 | 397.4436 | 0.399 | (3 4) | 351.30 | 351.9597 | −0.658 |
| (0 14) | 448.81 | 448.7108 | 0.096 | (3 5) | 390.15 | 390.9329 | −0.785 |
| (0 15) | 501.60 | 501.7664 | −0.162 | (3 6) | 431.66 | 432.5398 | −0.877 |
| (0 16) | 556.12 | 556.4650 | −0.343 | (3 7) | 475.60 | 476.5282 | −0.926 |
| (0 17) | 612.26 | 612.6711 | −0.407 | (3 8) | 521.76 | 522.6870 | −0.922 |
| (0 18) | 669.94 | 670.2580 | −0.318 | (3 9) | 569.99 | 570.8336 | −0.845 |
| (0 19) | 729.07 | 729.1059 | −0.035 | (3 10) | 620.13 | 620.8062 | −0.673 |
| (0 20) | 789.59 | 789.1010 | 0.484 | (3 11) | 672.08 | 672.4592 | −0.383 |
| (1 0) | 85.04 | 86.2903 | −1.253 | (3 12) | 725.71 | 725.6596 | 0.051 |
| (1 1) | 90.10 | 91.2120 | −1.112 | (4 0) | 304.64 | 303.0936 | 1.542 |
| (1 2) | 103.60 | 104.4256 | −0.830 | (4 1) | 340.46 | 339.6111 | 0.852 |
| (1 3) | 123.67 | 124.1949 | −0.528 | (4 2) | 377.14 | 376.8006 | 0.336 |
| (1 4) | 149.02 | 149.2855 | −0.270 | (4 3) | 415.88 | 415.9199 | −0.042 |
| (1 5) | 178.76 | 178.8451 | −0.081 | (4 4) | 456.86 | 457.1720 | −0.314 |
| (1 6) | 212.29 | 212.2602 | 0.029 | (4 5) | 500.03 | 500.5241 | −0.492 |
| (1 7) | 249.13 | 249.0662 | 0.063 | (4 6) | 545.30 | 545.8758 | −0.576 |
| (1 8) | 288.93 | 288.8958 | 0.029 | (4 7) | 592.55 | 593.1078 | −0.557 |
| (1 9) | 331.39 | 331.4483 | −0.056 | (4 8) | 641.68 | 642.0979 | −0.421 |
| (1 10) | 376.30 | 376.4701 | −0.174 | (4 9) | 692.58 | 692.7267 | −0.150 |
| (1 11) | 423.44 | 423.7425 | −0.301 | (4 10) | 745.16 | 744.8795 | 0.279 |
| (1 12) | 472.66 | 473.0733 | −0.412 | (4 11) | 799.34 | 798.4468 | 0.888 |
| (1 13) | 523.81 | 524.2908 | −0.479 | (4 12) | 855.03 | 853.3238 | 1.708 |
| (1 14) | 576.77 | 577.2395 | −0.469 | (5 0) | 389.60 | 388.0694 | 1.530 |
| (1 15) | 631.43 | 631.7769 | −0.351 | (5 1) | 433.35 | 432.1249 | 1.229 |
| (2 0) | 162.94 | 163.8041 | −0.864 | (5 2) | 476.53 | 475.7039 | 0.827 |
| (2 1) | 173.03 | 173.9391 | −0.910 | (5 3) | 520.61 | 520.1175 | 0.493 |
| (2 2) | 192.71 | 193.5571 | −0.849 | (5 4) | 566.10 | 565.8299 | 0.267 |
| (2 3) | 218.52 | 219.2953 | −0.773 | (5 5) | 613.16 | 612.9982 | 0.167 |
| (2 4) | 248.97 | 249.6923 | −0.717 | (5 6) | 661.86 | 661.6519 | 0.205 |
| (2 5) | 283.24 | 283.9316 | −0.695 | (5 7) | 712.16 | 711.7624 | 0.399 |
| (2 6) | 320.77 | 321.4770 | −0.703 | (5 8) | 764.04 | 763.2733 | 0.764 |
| (2 7) | 361.20 | 361.9377 | −0.735 | (5 9) | 817.44 | 816.1141 | 1.323 |

[a] Displaced oscillator basis quantum labels assigned to the optimized eigenvectors.
[b] Bending band origins from [19].
[c] Calculated energies.
[d] Difference between experimental and calculated energies.

bending band. This can be traced back to the need of including in the Hamiltonian higher order powers of the K angular momentum and its interaction with the bending vibration.

In Fig. 6 we show the quantum monodromy plot (upper left panel), the Birge-Sponer plot (upper right panel), the $\Delta B_{eff}$ (lower left panel), and the PR (lower right panel) for the NCNCS $\nu_7$ large amplitude bending mode. In the $\Delta B_{eff}$ case, a fit was performed making use of the expectation value of the number operator $\hat{n}$ in the eigenfunctions resulting from the fit to the vibrational band origins and computing the values of the $a_1$ and $a_2$ parameters in (18) that optimize the agreement with the observed $\Delta B_{eff}$ values reported in Tables 8 to 11 of Ref. [19]. The optimized parameter values are $a_1 = 2.39(4)$ MHz and $a_2 = 0.0108(4)$ MHz with a fit having an $rms = 1.29$ MHz. We explored the effect of a cubic term in the expansion but it provides a marginal improvement and the two-parameter expansion (18) already gives a fine result, achieving a satisfactory *rms*.

In Fig. 6, the change from a quadratic to a linear pattern in the quantum monodromy plot and the location of the Dixon dip [5] in the Birge-Sponer plot indicate that the critical energy of the monodromy -or the ESQPT critical energy- is around the $v_b = 3$ overtone, as already discussed in the literature [8,15,17,19]. In both plots the agreement between the reported data (green triangles) and the 2DVM results (blue circles) is good. We also include in the figure, as yellow circles, the values predicted by the GSRB model in Ref. [19]. The agreement achieved for the $\Delta B_{eff}$ is also very satisfactory.

The PR (lower right panel) in Fig. 6 makes evident the lack of significant localization effects in any basis for energies below the barrier. Nevertheless, the closest eigenstate to the critical energy $-v_b = 3$ overtone– is significantly more localized in the cylindrical oscillator basis, as predicted in recent works [73,87,88] for states close to the critical energy of the ESQPT.

The energy functional obtained making use of the coherent state approximation for this molecule, shown as an inset in the lower right panel of Fig. 6, provides an intuitive image for the po-

tential associated to the model, with a low barrier to linearity and it allows for a rough estimation of the height of this barrier at $\sim$ 225 cm$^{-1}$. Therefore, the different features shown in Fig. 6 confirm the nonrigid character of this molecule, which undergoes a bent-to-linear transition, in consonance with previous works [8,15,17,19].

## 4. Summary and conclusions

We analyze the bending vibrations of four different molecules making use of the 2DVM most general Hamiltonian that includes up to four-body interactions. The four molecular species have been selected trying to include examples of the different dynamics associated with the bending vibrational degree of freedom: linear, nonrigid, and bent. We present optimized algebraic spectroscopic parameters for each one of the cases, as well as the calculated bending spectrum and its comparison with reported values. The reader can find in the Supplementary Material section the full spectrum, including not yet measured or reported levels as well as a plot depicting the fit residuals as a function of energy. We use the model energies wave functions to compute the quantum monodromy, Birge-Sponer, and participation ratio for each case. In the latter case we illustrate the eigenstate localization in the two basis considered in the model.

Apart from its computational simplicity, one of the best 2DVM features is the possibility of encompassing, within a simple model, the full gamut of bending spectroscopic patterns that range from linear to bent, including the feature-rich nonrigid cases. We have focused particularly in nonrigid cases, where the bent-to-linear structural changes in the system, as it samples the top of the barrier to linearity for increasing excitation energies, can be considered as a perfect example of an ESQPT.

In a way, this work is a sequel of Refs. [8,56], where a systematic study of bending dynamics in molecular systems with and without ESQPT signatures was performed for the first time. In our case, we use a higher-order Hamiltonian to repeat the analysis, incorporating new reported data when possible, trying to improve the results, and casting some light upon the modeled physical systems. The extension of the algebraic Hamiltonian to include three- and four-body interactions has permitted us to model the available experimental data for the four molecules considered and, according to the *rms* of the fits (see Tab. 1), a satisfactory agreement is obtained between calculated and reported energies.

In particular, in the HNC case, the inclusion in the fit of a single three-body operator has dramatically improved the fit quality. As a bent molecule, we have considered the bending spectrum of $H_2S$, where the coupling with the rotational projection around the molecule-fixed $z$-axis in the Hamiltonian has been included to grapple with the rotational contribution. The results obtained in the fit to the $H_2S$ bending levels largely improves previously published results [56]; with an accuracy such that our predictions might be helpful for the assignment of new levels.

We have considered two nonrigid molecules, $Si_2C$ and NCNCS. In the first case we have obtained a fit within the experimental accuracy with only four parameters using one- and two-body interactions. In the NCNCS case, the epitome of a nonrigid molecule, we have also included results that reproduce rotational spectrum pa patterns associated with to the nonrigidity of the bending model. We have computed $\Delta B_{eff}$ obtaining in this case a satisfactory agreement too.

We have included the mean field limit energy functional for the bending degree of freedom of the nonrigid molecules under study using the intrinsic state formalism. Given the level of abstraction of the algebraic model, developed far from the traditional approach in phase space, this is a useful contribution as it provides a more intuitive handle to the obtained results. One should always take into consideration that this is a $1/N$ approximation, but still the bending energy functional shed light on the potential shape, the height of the linearity barriers, and the positions and number of minima.

Hence, we consider proved that the 4-body 2DVM Hamiltonian is a suitable effective Hamiltonian for the analysis of bending vibrations and it provides new venues to explore the ESQPT that occurs in the excitation spectrum of nonrigid molecular species. These results allow for an easier classification of the bending degree of freedom among the possible situations existing between the linear and bent limits, apart from being of great help in the assignment of quantum labels to highly-excited bending states, often quite a cumbersome task. Of course, one should always be aware of the model limits: it is a phenomenological model needing a minimal set of values, either experimental or extracted from experiment.

The programming codes used in this work are available upon request to the authors, and they will be published soon. In the Supplementary Material section, we provide predicted values for highly-excited bending levels of the molecules studied in this work, with the expectation that they could be of help in the measurement or assignment of experimental values. This is of particular importance in the case of nonrigid molecular species, where an improved knowledge of the critical energy region of the quantum monodromy –and, therefore, of the ESQPT– is of major importance and where we expect that our approach could facilitate the assignment of quantum labels. In addition to this, we also facilitate in the Supplementary Material section residual plots for the fits of the four molecules under study.

There are a number of developments that we are planning to undertake in a near future, fostered by the success of the four-body Hamiltonian. The full description of the vibrational spectrum of a molecule implies the simultaneous consideration of stretching and bending vibrational modes, as well as torsional, rocking, or other large amplitude modes. This can be naturally accomplished in the algebraic approach using coupled Lie algebras as shown in [82] for the case of two coupled benders or in [66–68,70] in the case of coupling of a bending and two stretching degrees of freedom. The latter works use an algebraic approach to obtain both energy levels and spectrum line intensities, a very important step for a right molecular characterization. The algebraic approach has performed very well in the characterization of spectrum energies and line intensities of experimental Franck-Condon [70,111–114] and Raman intensities [66–68]. In this respect we are currently paying heed to the modeling of highly excited bending progressions of HCN -with and without stretching excitations- to facilitate the assignment in a spectrum complicated by very large level density at high excitation energies.

In a different order, further developments of the model are currently being considered based on the promising results for the transition state in the isomerization of the [H,CN] system recently published in [71]. The new developments include the possibility of extending the model to simultaneously treat both isomer species. We will explore this model in comparison with the results obtained using the GSRB model for this same system [115]; and looking for inspiration in other, more sophisticate models as Refs. [116,117] and also Refs. [118,119], based on a formalism closer to the algebraic one. In particular, we are planning to explore a configuration mixing formalism akin to the one that has been successfully applied to nuclear systems [120].

## Declaration of Competing Interest

The authors declare that they have no known competing financial interests or personal relationships that could have appeared to influence the work reported in this paper.

## CRediT authorship contribution statement

**Jamil Khalouf-Rivera:** Conceptualization, Methodology, Software, Validation, Formal analysis, Investigation, Resources, Data curation, Writing - original draft, Writing - review & editing, Visualization. **Francisco Pérez-Bernal:** Conceptualization, Methodology, Software, Validation, Formal analysis, Investigation, Resources, Data curation, Writing - original draft, Writing - review & editing, Visualization, Supervision, Project administration, Funding acquisition. **Miguel Carvajal:** Conceptualization, Methodology, Validation, Investigation, Resources, Data curation, Writing - original draft, Writing - review & editing, Visualization, Supervision, Project administration, Funding acquisition.

## Acknowledgment

We thank useful discussion with Profs. Francesco Iachello, Renato Lemus, and Georg Mellau. This project has received funding from the European Union's Horizon 2020 research and innovation program under the Marie Skłodowska-Curie grant agreement No 872081 and from the Spanish National Research, Development, and Innovation plan (RDI plan) under the project PID2019-104002GB-C21. This work has also been partially supported by the Consejería de Conocimiento, Investigación y Universidad, Junta de Andalucía and European Regional Development Fund (ERDF), ref. SOMM17/6105/UGR, by the Ministerio de Ciencia, Innovación y Universidades (ref.COOPB20364), and by the Centro de Estudios Avanzados en Física, Matemáticas y Computación (CEAFMC) of the University of Huelva. JKR thanks support from the Youth Employment Initiative and the Youth Guarantee program supported by the European Social Fund. FPB and JKR thank the obtained support from the project UHU-1262561. Computing resources supporting this work were provided by the CEAFMC and Universidad de Huelva High Performance Computer (HPC@UHU) located in the Campus Universitario El Carmen and funded by FEDER/MINECO project UNHU-15CE-2848.

## Appendix A. Operator Matrix elements

*A0.1. Operator matrix elements in the dynamical symmetry (I)*

The diagonal operators in this dynamical symmetry are

Operator $\hat{n}^p$: $\langle [N]; n^\ell | \hat{n}^p | [N]; n^\ell \rangle = n^p$ for $p = 1, 2, 3, 4$.
Operator $\hat{\ell}^{2q}$: $\langle [N]; n^\ell | \hat{\ell}^{2q} | [N]; n^\ell \rangle = \ell^{2q}$ for $q = 1, 2$.
Operator $\hat{n}^p \hat{\ell}^{2q}$]: $\langle [N]; n^\ell | \hat{n}^p \ell^{2q} | [N]; n^\ell \rangle = n^p \ell^{2q}$ for $p = 1, 2$ and $q = 1$.

The non-diagonal matrix elements in this basis are

$SO(3)$ Casimir Operator $\hat{W}^2$:

$$\begin{aligned}\langle [N]; n_2^\ell | \hat{W}^2 | [N]; n_1^\ell \rangle =& \Big[ (N-n_1)(n_1+2) + (N-n_1+1)n_1 + \ell^2 \Big] \delta_{n_2,n_1} \\ & - \sqrt{(N-n_1+2)(N-n_1+1)(n_1+\ell)(n_1-\ell)}\, \delta_{n_2,n_1-2} \\ & - \sqrt{(N-n_1)(N-n_1-1)(n_1+\ell+2)(n_1-\ell+2)}\, \delta_{n_2,n_1+2}.\end{aligned}$$

Note that this is the main non-diagonal operator in this case and it is a band matrix as the non-zero matrix elements are located in the main and first diagonals only.

Operator $\hat{n}\hat{W}^2 + \hat{W}^2\hat{n}$: As the operator $\hat{n}$ is diagonal the matrix is also band diagonal with matrix elements

$$\begin{aligned}\langle [N]; n_2^\ell | \hat{n}\hat{W}^2 + \hat{W}^2\hat{n} | [N]; n_1^\ell \rangle =& 2n_1 \Big[ (N-n_1)(n_1+2) + (N-n_1+1)n_1 + \ell^2 \Big] \delta_{n_2,n_1} \\ & - (2n_1-2)\sqrt{(N-n_1+2)(N-n_1+1)(n_1+\ell)(n_1-\ell)}\, \delta_{n_2,n_1-2} \\ & - (2n_1+2)\sqrt{(N-n_1)(N-n_1-1)(n_1+\ell+2)(n_1-\ell+2)}\, \delta_{n_2,n_1+2}.\end{aligned}$$

Operator $\hat{\ell}^2\hat{W}^2$: This operator is computed for $\ell \neq 0$ multiplying the $\hat{W}^2$ operator matrix times $\ell^2$.
Operator $\hat{n}^2\hat{W}^2 + \hat{W}^2\hat{n}^2$: This is computed as the $\hat{n}\hat{W}^2 + \hat{W}^2\hat{n}$ operator.

$$\begin{aligned}\langle [N]; n_2^\ell | \hat{n}^2\hat{W}^2 + \hat{W}^2\hat{n}^2 | [N]; n_1^\ell \rangle =& 2n_1^2 \Big[ (N-n_1)(n_1+2) + (N-n_1+1)n_1 + \ell^2 \Big] \delta_{n_2,n_1} \\ & - [n_1^2 + (n_1-2)^2]\sqrt{(N-n_1+2)(N-n_1+1)(n_1+\ell)(n_1-\ell)}\, \delta_{n_2,n_1-2} \\ & - [n_1^2 + (n_1+2)^2]\sqrt{(N-n_1)(N-n_1-1)(n_1+\ell+2)(n_1-\ell+2)}\, \delta_{n_2,n_1+2}.\end{aligned}$$

Operator $\hat{W}^4$: This operator is computed as the matrix product of the $\hat{W}^2$ operator matrix times itself.
Operator $\hat{W}^2\hat{\bar{W}}^2 + \hat{\bar{W}}^2\hat{W}^2$: In this basis the only difference between the matrix elements of the $\hat{W}^2$ and $\hat{\bar{W}}^2$ operators is the sign of the non-diagonal contribution, which is positive in this case. The full operator is computed via matrix multiplication.

*A0.2. Operator matrix elements in the dynamical symmetry (II)*

The diagonal operators in this dynamical symmetry are

$SO(3)$ Casimir Operator $\hat{W}^2$: $\langle [N]; \omega\ell | \hat{W}^2 | [N]; \omega\ell \rangle = \omega(\omega+1)$.
Operator $\hat{\ell}^{2q}$: $\langle [N]; \omega\ell | \hat{\ell}^{2q} | [N]; \omega\ell \rangle = \ell^{2q}$ for $q = 1, 2$.
Operator $\hat{\ell}^2\hat{W}^2$: $\langle [N]; \omega\ell | \hat{\ell}^2\hat{W}^2 | [N]; \omega\ell \rangle = \ell^2\omega(\omega+1)$.
Operator $\hat{W}^4$: $\langle [N]; \omega\ell | \hat{W}^4 | [N]; \omega\ell \rangle = \omega^2(\omega+1)^2$.

The non-diagonal matrix elements in this basis are

Operator $\hat{n}$:

$$\begin{aligned}\langle [N]; \omega_2^\ell | \hat{n} | [N]; \omega_1^\ell \rangle =& \left\{ \frac{(N-\omega_1)[(\omega_1-\ell+2)(\omega_1-\ell+1) + (\omega_1+\ell+2)(\omega_1+\ell+1)]}{2(2\omega_1+1)(2\omega_1+3)} \right. \\ & \left. + \frac{(N+\omega_1+1)[(\omega_1+\ell)(\omega_1+\ell-1) + (\omega_1-\ell)(\omega_1-\ell-1)]}{2(2\omega_1+1)(2\omega_1-1)} \right\} \delta_{\omega_2,\omega_1} \\ & + \sqrt{\frac{(N-\omega_1)(N+\omega_1+3)(\omega_1-\ell+2)(\omega_1-\ell+1)(\omega_1+\ell+2)(\omega_1+\ell+1)}{(2\omega_1+1)(2\omega_1+3)^2(2\omega_1+5)}}\, \delta_{\omega_2,\omega_1+2} \\ & + \sqrt{\frac{(N-\omega_1+2)(N+\omega_1+1)(\omega_1-\ell)(\omega_1-\ell-1)(\omega_1+\ell)(\omega_1+\ell-1)}{(2\omega_1-3)(2\omega_1-1)^2(2\omega_1+1)}}\, \delta_{\omega_2,\omega_1-2}\end{aligned}$$

Note that this is the main non-diagonal operator in this case and it is again a band matrix with non-zero matrix elements located in the main and first diagonals only. The $\hat{n}$ matrix element in this basis are taken from [7] with a typo that has been corrected.

Operators $\hat{n}^2$, $\hat{n}^3$, and $\hat{n}^4$: These three operators are computed by matrix multiplication of the basic operator $\hat{n}$.
Operator $\hat{n}\hat{\ell}^2$: This operator is computed for $\ell \neq 0$ multiplying the $\hat{n}$ operator matrix times $\ell^2$.
Operator $\hat{n}\hat{W}^2 + \hat{W}^2\hat{n}$: As the operator $\hat{n}$ is band diagonal and $\hat{W}^2$ is diagonal, this operator matrix is also band diagonal with matrix elements

$$\begin{aligned}\langle [N];\omega_2\ell|\hat{n}\hat{W}^2+\hat{W}^2\hat{n}|[N];\omega_1\ell\rangle = 2\omega_1(\omega_1+1)\Bigg\{&\frac{(N-\omega_1)[(\omega_1-\ell+2)(\omega_1-\ell+1)+(\omega_1+\ell+2)(\omega_1+\ell+1)]}{2(2\omega_1+1)(2\omega_1+3)}\\ &+\frac{(N+\omega_1+1)[(\omega_1+\ell)(\omega_1+\ell-1)+(\omega_1-\ell)(\omega_1-\ell-1)]}{2(2\omega_1+1)(2\omega_1-1)}\Bigg\}\delta_{\omega_2,\omega_1}\\ &+[\omega_1(\omega_1+1)+(\omega_1+2)(\omega_1+3)]\\ &\times\sqrt{\frac{(N-\omega_1)(N+\omega_1+3)(\omega_1-\ell+2)(\omega_1-\ell+1)(\omega_1+\ell+2)(\omega_1+\ell+1)}{(2\omega_1+1)(2\omega_1+3)^2(2\omega_1+5)}}\delta_{\omega_2,\omega_1+2}\\ &+[(\omega_1-2)(\omega_1-1)+\omega_1(\omega_1+1)]\\ &\times\sqrt{\frac{(N-\omega_1+2)(N+\omega_1+1)(\omega_1-\ell)(\omega_1-\ell-1)(\omega_1+\ell)(\omega_1+\ell-1)}{(2\omega_1-3)(2\omega_1-1)^2(2\omega_1+1)}}\delta_{\omega_2,\omega_1-2}\end{aligned}$$

Operator $\hat{n}^2\hat{W}^2 + \hat{W}^2\hat{n}^2$: This is computed in the same way that the $\hat{n}\hat{W}^2 + \hat{W}^2\hat{n}$ operator but taking into account that the $\hat{n}^2$ operator is double banded. Therefore the operator matrix elements can be expressed as follow

$$\begin{aligned}\langle [N];\omega_2\ell|\hat{n}^2\hat{W}^2+\hat{W}^2\hat{n}^2|[N];\omega_1\ell\rangle = 2\omega_1(\omega_1+1)&[\hat{n}^2]_{\omega_1,\omega_1}\delta_{\omega_2,\omega_1}\\ &+[\omega_1(\omega_1+1)+(\omega_1+2)(\omega_1+3)][\hat{n}^2]_{\omega_1,\omega_1+2}\delta_{\omega_2,\omega_1+2}\\ &+[(\omega_1-2)(\omega_1-1)+\omega_1(\omega_1+1)][\hat{n}^2]_{\omega_1,\omega_1-2}\delta_{\omega_2,\omega_1-2}\\ &+[\omega_1(\omega_1+1)+(\omega_1+4)(\omega_1+5)][\hat{n}^2]_{\omega_1,\omega_1+4}\delta_{\omega_2,\omega_1+4}\\ &+[(\omega_1-4)(\omega_1-3)+\omega_1(\omega_1+1)][\hat{n}^2]_{\omega_1,\omega_1-4}\delta_{\omega_2,\omega_1-4},\end{aligned}$$

where $[\hat{n}^2]_{\omega_i,\omega_j}$ are the $\hat{n}^2$ operator matrix elements.

Operator $\hat{W}^2\hat{\overline{W}}^2 + \hat{\overline{W}}^2\hat{W}^2$: In this basis we need first to compute the matrix elements of the $\hat{\overline{W}}^2$ making use of Eqs. (37) and (38) of Ref[7].

$$\langle [N];\omega_2\ell_2|\hat{R}_-|[N];\omega_1\ell_1\rangle = A_{\omega_1,\ell_1}\,\delta_{\omega_2,\omega_1}\delta_{\ell_2,\ell_1-1} + B_{\omega_1,\ell_1}\,\delta_{\omega_2,\omega_1-2}\delta_{\ell_2,\ell_1-1} + C_{\omega_1,\ell_1}\,\delta_{\omega_2,\omega_1+2}\delta_{\ell_2,\ell_1-1},$$

where

$$A_{\omega,\ell} = \frac{(2N+3)(2\ell+1)}{(2\omega-1)(2\omega+3)}\sqrt{(\omega+\ell)(\omega-\ell+1)/2}$$

$$B_{\omega,\ell} = -\sqrt{\frac{2(N+\omega+1)(N-\omega+2)(\omega+\ell)(\omega-\ell)(\omega+\ell-1)(\omega+\ell-2)}{(2\omega+1)(2\omega-1)^2(2\omega-3)}}$$

$$C_{\omega,\ell} = \sqrt{\frac{2(N+\omega+3)(N-\omega)(\omega+\ell+1)(\omega-\ell+1)(\omega-\ell+2)(\omega-\ell+3)}{(2\omega+1)(2\omega+3)^2(2\omega+5)}}.$$

The previous result can be used for the derivation of an expression for the $\hat{R}_+$ operator matrix elements

$$\begin{aligned}\langle [N];\omega_2\ell_2|\hat{R}_-|[N];\omega_1\ell_1\rangle^\dagger =&\langle [N];\omega_1\ell_1|\hat{R}_+|[N];\omega_2\ell_2\rangle\\ =&A_{\omega_2,\ell_2+1}\,\delta_{\omega_1,\omega_2}\delta_{\ell_1,\ell_2+1} + B_{\omega_2+2,\ell_2+1}\,\delta_{\omega_1,\omega_2-2}\delta_{\ell_1,\ell_2+1}\\ &+C_{\omega_2-2,\ell_2+1}\,\delta_{\omega_1,\omega_2+2}\delta_{\ell_1,\ell_2+1}.\end{aligned}$$

The upper diagonal matrix elements of the Casimir operator $\hat{\overline{W}}^2 = \hat{R}_+\hat{R}_- + \hat{\ell}^2$ can then be expressed as

$$\begin{aligned}\langle [N];\omega_2\ell|\hat{\overline{W}}^2|[N];\omega_1\ell\rangle = &(A^2_{\omega_1,\ell_1} + B^2_{\omega_1,\ell_1} + C^2_{\omega_1,\ell_1})\,\delta_{\omega_2,\omega_1}\\ &+(A_{\omega_1,\ell}\,B_{\omega_1+2,\ell} + C_{\omega_1,\ell}\,A_{\omega_1+2,\ell})\,\delta_{\omega_2,\omega_1+2}\\ &+C_{\omega_1,\ell}\,B_{\omega_1+4,\ell}\,\delta_{\omega_2,\omega_1+4},\end{aligned}$$

and the lower diagonal matrix elements can be computed considering that the upper and lower bandwidths are the same.

The $\hat{W}^2\hat{\overline{W}}^2 + \hat{\overline{W}}^2\hat{W}^2$ operator is then computed as for the $\hat{n}^2\hat{W}^2 + \hat{W}^2\hat{n}^2$ operator

$$\langle [N];\omega_2\ell|\hat{W}^2\hat{\overline{W}}^2+\hat{\overline{W}}^2\hat{W}^2|[N];\omega_1\ell\rangle = 2\omega_1(\omega_1+1)\,[\hat{\overline{W}}^2]_{\omega_1,\omega_1}\delta_{\omega_2,\omega_1}$$

$$+[\omega_1(\omega_1+1)+(\omega_1+2)(\omega_1+3)][\hat{\overline{W}}^2]_{\omega_1,\omega_1+2}\delta_{\omega_2,\omega_1+2}$$
$$+[(\omega_1-2)(\omega_1-1)+\omega_1(\omega_1+1)][\hat{\overline{W}}^2]_{\omega_1,\omega_1-2}\delta_{\omega_2,\omega_1-2}$$
$$+[\omega_1(\omega_1+1)+(\omega_1+4)(\omega_1+5)][\hat{\overline{W}}^2]_{\omega_1,\omega_1+4}\delta_{\omega_2,\omega_1+4}$$
$$+[(\omega_1-4)(\omega_1-3)+\omega_1(\omega_1+1)][\hat{\overline{W}}^2]_{\omega_1,\omega_1-4}\delta_{\omega_2,\omega_1-4},$$

where $[\hat{\overline{W}}^2]_{\omega_i,\omega_j}$ are the $\hat{\overline{W}}^2$ operator matrix elements.

## Appendix B. Coherent state approach results

The matrix elements of the different operators in Hamiltonian (10), $\langle\hat{O}\rangle_{c.s.}=\langle[N];\mathbf{r}|\hat{O}|[N];\mathbf{r}\rangle$ for one- to four-body operators are

- **One-body operator:**
  - $\langle\hat{n}\rangle_{c.s.}=N\frac{r^2}{1+r^2}$
- **Two-body operators:**
  - $\langle\hat{n}^2\rangle_{c.s.}=N\frac{r^2}{1+r^2}+N(N-1)\frac{r^4}{(1+r^2)^2}$
  - $\langle\hat{\ell}^2\rangle_{c.s.}=\langle\hat{n}\rangle_{c.s.}$
  - $\langle\hat{W}^2\rangle_{c.s.}=2N+N(N-1)\frac{4r^2}{(1+r^2)^2}$
- **Three-body operators:**
  - $\langle\hat{n}^3\rangle_{c.s.}=N\frac{r^2}{1+r^2}+3N(N-1)\frac{r^4}{(1+r^2)^2}+N(N-1)(N-2)\frac{r^6}{(1+r^2)^3}$
  - $\langle\hat{n}\hat{\ell}^2\rangle_{c.s.}=\langle\hat{n}^2\rangle_{c.s.}$
  - $\langle\hat{n}\hat{W}^2+\hat{W}^2\hat{n}\rangle_{c.s.}=4N\frac{r^2}{1+r^2}+4N(N-1)\frac{r^4}{(1+r^2)^2}+12N(N-1)\frac{r^2}{(1+r^2)^2}+8N(N-1)(N-2)\frac{r^4}{(1+r^3)^3}$
- **Four-body operators:**
  - $\langle\hat{n}^4\rangle_{c.s.}=N\frac{r^2}{1+r^2}+7N(N-1)\frac{r^4}{(1+r^2)^2}+6N(N-1)(N-2)\frac{r^6}{(1+r^2)^3}+N(N-1)(N-2)(N-3)\frac{r^8}{(1+r^2)^4}$
  - $\langle\hat{n}^2\hat{\ell}^2\rangle_{c.s.}=\langle\hat{n}^3\rangle_{c.s.}$
  - $\langle\hat{\ell}^4\rangle_{c.s.}=N\frac{r^2}{1+r^2}+3N(N-1)\frac{r^4}{(1+r^2)^2}$
  - $\langle\hat{\ell}^2\hat{W}^2\rangle_{c.s.}=2N\frac{r^2}{1+r^2}+4N(N-1)\frac{r^4+r^2}{(1+r^2)^2}+4N(N-1)(N-2)\frac{r^4}{(1+r^2)^3}$
  - $\langle\hat{n}^2\hat{W}^2+\hat{W}^2\hat{n}^2\rangle_{c.s.}=4N\frac{r^2}{1+r^2}+N(N-1)\frac{12r^4+16r^2}{(1+r^2)^2}+N(N-1)(N-2)\frac{4r^6+28r^4}{(1+r^2)^3}+N(N-1)(N-2)(N-3)\frac{8r^6}{(1+r^2)^4}$
  - $\langle\hat{W}^4\rangle_{c.s.}=4N(2N-1)+24N(N-1)\frac{r^2}{(1+r^2)^2}+32N(N-1)(N-2)\frac{r^4+r^2}{(1+r^2)^3}+16N(N-1)(N-2)(N-3)\frac{r^4}{(1+r^2)^4}$
  - $\frac{1}{2}\left\langle\hat{W}^2\hat{\overline{W}}^2+\hat{\overline{W}}^2\hat{W}^2\right\rangle_{c.s.}=4N+N(N-1)\frac{4r^4+28r^2}{(1+r^2)^2}+8N(N-1)(N-2)\frac{r^4+r^2}{(1+r^2)^3}$

The connection of the energy functional with results obtained using the traditional analysis in phase space is hindered by the need of a connection between the unitless $r$ variable and the physical bending coordinate. A connection has been worked out for the two dynamical symmetries [8,29], with a simple linear relationship based on the molecular G matrix elements. However, it is necessary to look for a more elaborate relationship between the classical coordinate resulting from the coherent state approach and the physical coordinate valid for more general cases. Still, we can obtain a qualitative description of the system potential by directly connecting the $r$ intrinsic approach classical variable to the deviation of linearity angle, $\theta(rad)=\frac{\theta_e(rad)}{r_{\min}}r$, making use of the experimental information on the molecular equilibrium structure. We have used the intrinsic state approach only in the two nonrigid molecules, $Si_2C$ and NCNCS. In this way the energy functional has the minimum located at the right position, and the figure offers a pictorial and intuitive perspective to the obtained results and a qualitative image of the potential shape. We are planning to work on a more involved scaling in a future work.

## Supplementary material

Supplementary material associated with this article can be found, in the online version, at doi:10.1016/j.jqsrt.2020.107436

## References


[1] Quapp W, Winnewisser B. What you thought you already knew about the bending motion of triatomic molecules. J Math Chem 1993;14:259–85.
[2] Jensen P, Spanner M, Bunker P. The CO2 molecule is never linear. J Mol Struct 2020;1212. 128–087
[3] Thorson W, Nakagawa I. Dynamics of the quasi-linear molecule. J Chem Phys 1960;33:994–1004.
[4] Herzberg G. Molecular spectra and molecular structure, vol. III: electronic spectra and electronic structure of polyatomic molecules. Van Nostrand Reinhold, New York; 1966.
[5] Dixon RN. Higher vibrational levels of a Bent triatomic molecule. Trans Faraday Soc 1964;60:1363–8.
[6] Iachello F, Pérez-Bernal F, Vaccaro P. A novel algebraic scheme for describing nonrigid molecules. Chem Phys Lett 2003;375:309–20.
[7] Pérez-Bernal F, Iachello F. Algebraic approach to two-Dimensional systems: shape phase transitions, monodromy, and thermodynamic quantities. Phys Rev A 2008;77:032–115.
[8] Larese D, Iachello F. A study of quantum phase transitions and quantum monodromy in the bending motion of non-Rigid molecules. J Mol Struct 2011;1006:611–28.
[9] Hougen JT, Bunker P, Johns J. The vibration-Rotation problem in triatomic molecules allowing for a large-Amplitude bending vibration. J Mol Spectrosc 1970;34:136–72.
[10] Bunker P, Landsberg B. The rigid bender and semirigid bender models for the rotation-vibration hamiltonian. J Mol Spectrosc 1977;67:374–85.
[11] Ross S. OCCCS, NCNCS, NCNCO, And NCNNN as semirigid benders. J Mol Spectrosc 1988;132:48–79.
[12] Jensen P. A new morse oscillator-Rigid bender internal dynamics (MORBID) hamiltonian for triatomic molecules. J Mol Spectrosc 1988;128:478–501.
[13] Bates L. Monodromy in the champagne bottle. Zeitschrift für Angewandte Mathematik und Physik 1991;42:837–47.
[14] Child MS. Quantum states in a champagne bottle. J Phys A: Math and General 1998;31:657–70.
[15] Winnewisser M, Winnewisser B, Medvedev I, Lucia FD, Ross S, Bates L. The hidden kernel of molecular quasi-Linearity: quantum monodromy. J Mol Struct 2006;798:1–26.
[16] Child MS, Weston T, Tennyson J. Quantum monodromy in the spectrum of H2O and other systems: new insight into the level structure of quasi-Linear molecules. Mol Phys 1999;96:371–9.
[17] Winnewisser B, Winnewisser M, Medvedev I, Behnke M, De Lucia F, Ross S, et al. Experimental confirmation of quantum monodromy: the millimeter wave spectrum of cyanogen isothiocyanate NCNCS. Phys Rev Lett 2005;95:243002.
[18] Zobov N, Shirin S, Polyansky O, Tennyson J, Coheur P-F, Bernath P, et al. Monodromy in the water molecule. Chem Phys Lett 2005;414:193–7.
[19] Winnewisser B, Winnewisser M, Medvedev I, De Lucia F, Ross S, Koput J. Analysis of the FASSST rotational spectrum of NCNCS in view of quantum monodromy. Phys Chem Chem Phys 2010;12:8158–89.
[20] Winnewisser M, Winnewisser BP, De Lucia FC, Tokaryk DW, Ross SC, Billinghurst BE. Pursuit of quantum monodromy in the far-Infrared and mid-Infrared spectra of NCNCS using synchrotron radiation. Phys Chem Chem Phys 2014;16:17373–407.
[21] Reilly N, Changala P, Baraban J, Kokkin D, Stanton J, McCarthy M. Communication: the ground electronic state of si2c: rovibrational level structure, quantum monodromy, and astrophysical implications. J Chem Phys 2015;142:231101.
[22] Iachello F. Lie algebras and applications (lecture notes in physics), 708. Springer, Berlin; 2006.
[23] Iachello F, Arima A. The interacting boson model. Cambridge University Press, Cambridge; 1987.
[24] Iachello F. Dynamic symmetries and supersymmetries in nuclear physics. Rev Mod Phys 1993;65:569–76.
[25] Bijker R, Iachello F, Leviatan A. Algebraic models of hadron structure. I. nonstrange baryons. Ann Phys 1994;236:69–116.
[26] Iachello F, Levine R. Algebraic theory of molecules. Oxford University Press, New York; 1995.
[27] Iachello F. Algebraic methods for molecular rotation-Vibration spectra. Chem Phys Lett 1981;78:581–5.
[28] Iachello F, Oss S. Algebraic approach to molecular spectra: two dimensional problems. J Chem Phys 1996;104:6956–63.
[29] Pérez-Bernal F, Santos L, Vaccaro P, Iachello F. Spectroscopic signatures of nonrigidity: algebraic analyses of infrared and raman transitions in nonrigid species. Chem Phys Lett 2005;414:398–404.
[30] Cejnar P, Iachello F. Phase structure of interacting Boson models in arbitrary dimension. J Phys A: Math and Theor 2007;40:581.
[31] Gilmore R. The classical limit of quantum nonspin systems. J Math Phys 1979;20:891–3.
[32] Cejnar P, Jolie J. Quantum phase transitions in the interacting Boson model. Prog Part Nucl Phys 2009;62:210–56.
[33] Casten R. Quantum phase transitions and structural evolution in nuclei. Prog Part Nucl Phys 2009;62:183–209.
[34] Cejnar P, Jolie J, Casten R. Quantum phase transitions in the shapes of atomic nuclei. Rev Mod Phys 2010;82:2155–212.
[35] Zhang Y, Pan F, Liu Y-X, Draayer J. The e(2) symmetry and quantum phase transition in the two-Dimensional limit of the vibron model. J Phys B–At Mol Opt 2010;43:225101.
[36] Pérez-Fernández P, Arias J, García-Ramos JE, Pérez-Bernal F. Finite-Size corrections in the bosonic algebraic approach to two-Dimensional systems. Phys Rev A 2011;83:062125.
[37] Calixto M, Romera E, del Real R. Parity-Symmetry-Adapted coherent states and entanglement in quantum phase transitions of vibron models. J Phys A: Math Theor 2012;45:365301.
[38] Calixto M, del Real R, Romera E. Husimi distribution and phase-space analysis of a vibron-model quantum phase transition. Phys Rev A 2012;86:032508.
[39] de los Santos F, Romera E. Revival times at quantum phase transitions. Phys Rev A 2013;87:013424.
[40] Castaños O, Calixto M, Pérez-Bernal F, Romera E. Identifying the order of a quantum phase transition by means of wehrl entropy in phase space. Phys Rev E 2015;92:052106.
[41] Cejnar P, Macek M, Heinze S, Jolie J, Dobeš J. Monodromy and excited-State quantum phase transitions in integrable systems: collective vibrations of nuclei. J Phys A: Math and General 2006;39:L515–21.
[42] Caprio M, Cejnar P, Iachello F. Excited state quantum phase transitions in many-Body systems. Ann Phys 2008;323:1106–35.
[43] Pérez-Fernández P, Relaño A, Arias JM, Cejnar P, Dukelsky J, García-Ramos JE. Excited-State phase transition and onset of chaos in quantum optical models. Phys Rev E 2011;83:046208.
[44] Bastidas V, Pérez-Fernández P, Vogl M, Brandes T. Quantum criticality and dynamical instability in the kicked-top model. Phys Rev Lett 2014;112:140408.
[45] Puebla R, Hwang M-J, Plenio MB. Excited-State quantum phase transition in the rabi model. Phys Rev A 2016;94:023835.
[46] Pérez-Fernández P, Relaño A, Arias JM, Dukelsky J, García-Ramos JE. Decoherence due to an excited-state quantum phase transition in a two-level boson model. Phys Rev A 2009;80:032111.
[47] Yuan Z-G, Zhang P, Li S-S, Jing J, Kong L-B. Scaling of the berry phase close to the excited-State quantum phase transition in the lipkin model. Phys Rev A 2012;85:044102.
[48] Kopylov W, Brandes T. Time delayed control of excited state quantum phase transitions in the lipkin–meshkov–glick model. New J Phys 2015;17(10):103031. doi:10.1088/1367-2630/17/10/103031.
[49] Wang Q, Pérez-Bernal F. Excited-State quantum phase transition and the quantum-Speed-Limit time. Phys Rev A 2019;100:022118.
[50] Wang Q, Pérez-Bernal F. Probing an excited-State quantum phase transition in a quantum many-Body system via an out-of-Time-Order correlator. Phys Rev A 2019;100:062113.
[51] Brandes T. Excited-State quantum phase transitions in dicke superradiance models. Phys Rev E 2013;88:032133.
[52] Kloc M, Stránský P, Cejnar P. Quantum quench dynamics in dicke superradiance models. Phys Rev A 2018;98:013836.
[53] Cejnar P., Stránský P., Macek M., Kloc M.. Excited-state quantum phase transitions. 2020. arXiv:2011.01662.
[54] Kloc M, Stránský P, Cejnar P. Monodromy in Dicke Superradiance. J Phys A: Math and Theor 2017;50. 315–205
[55] Wang Q, Quan HT. Probing the excited-State quantum phase transition through statistics of loschmidt echo and quantum work. Phys Rev E 2017;96:032142.
[56] Larese D, Pérez-Bernal F, Iachello F. Signatures of quantum phase transitions and excited state quantum phase transitions in the vibrational bending dynamics of triatomic molecules. J Mol Struct 2013;1051:310–27.
[57] Dietz B, Iachello F, Miski-Oglu M, Pietralla N, Richter A, von Smekal L, et al. Lifshitz and excited-State quantum phase transitions in microwave dirac billiards. Phys Rev B 2013;88:104101.
[58] Zhao L, Jiang J, Tang T, Webb M, Liu Y. Dynamics in spinor condensates tuned by a microwave dressing field. Phys Rev A 2014;89:023608.
[59] Evers F, Mirlin A. Anderson transitions. Rev Mod Phys 2008;80:1355–1417.
[60] Dieperink AEL, Scholten O, Iachello F. Classical limit of the interacting-Boson model. Phys Rev Lett 1980;44:1747–50.
[61] Leviatan A, Kirson M. Intrinsic and collective structure of an algebraic model of molecular rotation-Vibration spectra. Ann Phys 1988;188:142–85.
[62] Roosmalen OV, Dieperink A, Iachello F. A dynamic algebra for rotation-Vibration spectra of complex molecules. Chem Phys Lett 1982;85:32–6.
[63] Iachello F, Oss S, Lemus R. Linear four-Atomic molecules in the vibron model. J Mol Spectrosc 1991;149:132–51.
[64] Oss S, Temsamani MA. Intensities of infrared transitions in the two-Dimensional algebraic model. J Chem Phys 1998;108:1773–9.
[65] Abbouti Temsamani M, Champion J-M, Oss S. Infrared transition intensities in acetylene: an algebraic approach. J Chem Phys 1999;110:2893–902.
[66] Sánchez-Castellanos M, Lemus R, Carvajal M, Pérez-Bernal F, Fernández J. A study of the raman spectrum of CO2 using an algebraic approach. Chem Phys Lett 2012;554:208–13.
[67] Lemus R, Sánchez-Castellanos M, Pérez-Bernal F, Fernández JM, Carvajal M. Simulation of the raman spectra of CO2: bridging the gap between algebraic models and experimental spectra. J Chem Phys 2014;141:054–306.

[68] Bermúdez-Montaña M, Carvajal M, Pérez-Bernal F, Lemus R. An Algebraic Alternative for the Accurate Simulation of $CO_2$Raman Spectra. J Raman Spectrosc 2020;51:569–83.
[69] Sako T, Aoki D, Yamanouchi K, Iachello F. Algebraic force-Field hamiltonian expansion approach to linear polyatomic molecules. J Chem Phys 2000;113:6063–9.
[70] Ishikawa H, Toyosaki H, Mikami N, Pérez-Bernal F, Vaccaro P, Iachello F. Algebraic analysis of bent-from-Linear transition intensities: the vibronically resolved emission spectrum of methinophosphide (HCP). Chem Phys Lett 2002;365:57–68.
[71] Khalouf-Rivera J, Carvajal M, Santos L, Pérez-Bernal F. Calculation of transition state energies in the HCN-HNC isomerization with an algebraic model. J Phys Chem A 2019;123:9544–51.
[72] Pérez-Bernal F, Álvarez-Bajo O. Anharmonicity effects in the bosonic u(2)-SO(3) excited-State quantum phase transition. Phys Rev A 2010;81:050–101.
[73] Pérez-Bernal F, Santos L. Effects of excited state quantum phase transitions on system dynamics. Fortschr Phys 2017;65:1600035.
[74] Rodriguez-Arcos M, Lemus R. Unitary group approach for effective potentials in 2D systems: application to carbon suboxide C3O2. Chem Phys Lett 2018;713:266–71.
[75] Estévez-Fregoso MM, Lemus R. Connection between the su(3) algebraic and configuration spaces: bending modes of linear molecules. Mol Phys 2018;116:2374–95.
[76] Estévez-Fregoso MM, Arias JM, Gómez-Camacho J, Lemus R. An Approach to Establish a Connection between Algebraic and Configuration Spaces: $su(\nu+1)$Algebraic Model for Vibrational Excitations. Mol Phys 2018;116:2254–69.
[77] Stránský P, Macek M, Cejnar P. Excited-State quantum phase transitions in systems with two degrees of freedom: level density, level dynamics, thermal properties. Ann Phys 2014;345:73–97.
[78] Stránský P, Macek M, Leviatan A, Cejnar P. Excited-State quantum phase transitions in systems with two degrees of freedom: II. finite-Size effects. Ann Phys 2015;356:57–82.
[79] Iachello F, Pérez-bernal F. Bending vibrational modes of ABBA molecules: algebraic approach and its classical limit. Mol Phys 2008;106(2–4):223–31.
[80] Iachello F, Pérez-Bernal F. A novel algebraic scheme for describing coupled benders in tetratomic molecules. J Phys Chem A 2009;113:13273–86.
[81] Pérez-Bernal F, Fortunato L. Phase diagram of coupled benders within a u(3)xu(3) algebraic approach. Phys Lett A 2012;376:236–44.
[82] Larese D, Caprio M, Pérez-Bernal F, Iachello F. A study of the bending motion in tetratomic molecules by the algebraic operator expansion method. J Chem Phys 2014;140:014–304.
[83] Calixto M, Pérez-Bernal F. Entanglement in shape phase transitions of coupled molecular benders. Phys Rev A 2014;89:032–126.
[84] Iachello F, Dietz B, Miski-Oglu M, Richter A. Algebraic theory of crystal vibrations: singularities and zeros in vibrations of one- and two-Dimensional lattices. Phys Rev B 2015;91:214–307.
[85] Frank A, Isacker PV. Algebraic methods in molecular and nuclear structure physics. John Wiley and Sons, New York; 1994.
[86] Yamada K, Winnewisser M. A parameter to quantify molecular quasilinearity. Z Naturforsch A 1976;31:139–44.
[87] Santos L, Pérez-Bernal F. Structure of eigenstates and quench dynamics at an excited-State quantum phase transition. Phys Rev A 2015;92:050101.
[88] Santos L, Távora M, Pérez-Bernal F. Excited-State quantum phase transitions in many-Body systems with infinite-Range interaction: localization, dynamics, and bifurcation. Phys Rev A 2016;94:012–113.
[89] Zelevinsky V, Brown B, Frazier N, Horoi M. The nuclear shell model as a testing ground for many-Body quantum chaos. Phys Rep 1996;276:85–176.
[90] Izrailev F. Simple models of quantum chaos: spectrum and eigenfunctions. Phys Rep 1990;196:299–392.
[91] Anderson E, Bai Z, Bischof C, Blackford S, Demmel J, Dongarra J, et al. LAPACK Users' Guide. third. Philadelphia, PA: Society for Industrial and Applied Mathematics; 1999. 0-89871-447-8 (paperback)
[92] Barker V, Blackford LS, et al. LAPACK95 Users' Guide Tech. Rep.; 2001. Netlib.org
[93] James F, Roos M. MINUIT - System for function minimization and analysis of parameter errors and correlations. Comput Phys Commun 1975;10(6):343–67.
[94] Mellau G. Complete Experimental Rovibrational Eigenenergies of HNC up to 3743$cm^{-1}$ above the Ground State. J Chem Phys 2010;133:164–303.
[95] Carvajal M, Lemus R. Toward a Global Analysis Method Based on Anharmonic Ladder Operators: Application to Hydrogen Sulfide ($H_2{}^32S$). J Phys Chem A 2015;119:12823–38.
[96] Lechuga-Fossat L, Flaud J-M, Camy-Peyret C, Johns JWC. The spectrum of natural hydrogen sulfide between 2150 and 2950 cm-1. Can J Phys 1984;62(12):1889–923.
[97] Ulenikov O, Malikova A, Koivusaari M, Alanko S, Anttila R. High Resolution Vibrational-rotational Spectrum of $H_2S$ in the Region of the $\nu_2$Fundamental Band. J Mol Spectrosc 1996;176(2):229–35.
[98] Brown L, Crisp J, Crisp D, Naumenko O, Smirnov M, Sinitsa L, et al. The Absorption Spectrum of H2S Between 2150 and 4260 cm-1: Analysis of the Positions and Intensities in the First ($2\nu_2$, $\nu_1$, and $\nu_3$) and Second ($3\nu_2$, $\nu_1+\nu_2$, and $\nu_2+\nu_3$) Triad Regions. J Mol Spectrosc 1998;188(2):148–74.
[99] Ulenikov O, Liu A-W, Bekhtereva E, Gromova O, Hao L-Y, Hu S-M. High-Resolution Fourier Transform Spectrum of $H_2S$in the Region of the Second Hexade. J Mol Spectrosc 2005;234:270–8.
[100] Azzam A, Yurchenko S, Tennyson J, Martin-Drumel M-A, Pirali O. Terahertz spectroscopy of hydrogen sulfide. J Quant Spectrosc Rad Trans 2013;130:341–51.
[101] Ulenikov O, Bekhtereva E, Gromova O, Zhang F, Raspopova N, Sydow C, et al. Ro-Vibrational Analysis of the First Hexad of Hydrogen Sulfide: Line Position and Strength Analysis of the $4\nu2$ Band of $H_2{}^32S$ and $H_2{}^34S$ for HITRAN Applications. J Quant Spectrosc Radiat Trans 2020;255:107–236.
[102] Álvarez-Bajo O, Carvajal M, Pérez-Bernal F. An Approach to Global Rovibrational Analysis Based on Anharmonic Ladder Operators: Application to Hydrogen Selenide $H_2{}^{80}Se$. Chem Phys 2012;392(1):63–70.
[103] Kafafi ZH, Hauge RH, Fredin L, Margrave JL. Infrared Matrix Isolation Spectrum of the Disilicon Carbide ($Si_2C$) Molecule. J Phys Chem 1983;87:797–800.
[104] Rittby CML. An Ab Initio Study of the Structure and infrared Spectrum of $Si_2C$. J Chem Phys 1991;95(8):5609–11.
[105] Presilla-Márquez JD, Graham WRM. Fourier Transform Vibrational Spectroscopy of $Si_2C$ in Solid Ar. J Chem Phys 1991;95(8):5612–17.
[106] McCarthy M, Baraban J, Changala P, Stanton J, Martin-Drumel M-A, Thorwirth S, et al. Discovery of a missing link: detection and structure of the elusive disilicon carbide cluster. J Phys Chem Lett 2015;6:2107–11.
[107] Cernicharo J, McCarthy MC, Gottlieb CA, Agúndez M, Prieto LV, Baraban JH, et al. Discovery os SiCSi in IRC+10216: AMissing Link between Gas and dust Carriers of Si–C Bonds. Astrophys J 2015;806:L3.
[108] Koput J. Ab Initio Potential Energy Surface and Vibration-Rotation Energy Levels of Disilicon Carbide, $CSi_2$. J Mol Spectr 2017;342:83–91.
[109] King MA, Kroto HW, Landsberg B. Microwave spectrum of the quasi-linear molecule, cyanogen isothiocyanate (NCNCS). J Mol Spectrosc 1985;113(1):1–20.
[110] Iachello F, Levine R. Algebraic theory of molecules. Oxford University Press, Oxford; 1995.
[111] Müller T, Dupré P, Vaccaro P, Pérez-Bernal F, Ibrahim M, Iachello F. Algebraic Approach for the Calculation of Polyatomic Franck-Condon Factors.: Application to the Vibronically Resolved Emission Spectrum of $S_2O$. Chem Phys Lett 1998;292(3):243–53.
[112] Müller T, Vaccaro PH, Pérez-Bernal F, Iachello F. The Vibronically-resolved Emission Spectrum of Disulfur Monoxide ($S_2O$): An Algebraic Calculation and Quantitative Interpretation of Franck-Condon Transition Intensities. J Chem Phys 1999;111(11):5038–55.
[113] Müller T, Vaccaro P, Pérez-Bernal F, Iachello F. Algebraic Approach for the Calculation of Polyatomic Franck-Condon Factors: Application to the Vibronically Resolved Absorption Spectrum of Disulfur Monoxide ($S_2O$). Chem Phys Lett 2000;329(3):271–82.
[114] Iachello F, Pérez-Bernal F, Müller T, Vaccaro PH. A Quantitative Study of Non-Condon Effects in the $S_2O$ C-X Emission Spectrum. J Chem Phys 2000;112(15):6507–10.
[115] Ross S, Bunker P. The potential function for HCN-CNH isomerization. J Mol Spectrosc 1983;101(1):199–211.
[116] Odaka TE, Jensen P, Hirano T. The Double Renner Effect: A Theoretical Study of the MgNC/MgCN Isomerization in the Ã 2Π Electronic State. J Mol Struct 2006;795(1):14–41.
[117] Mellau GC, Winnewisser BP, Winnewisser M. Near infrared emission spectrum of HCN. J Mol Spectrosc 2008;249(1):23–42.
[118] Barnes GL, Kellman ME. Communication: Effective Spectroscopic Hamiltonian for Multiple Minima with above Barrier Motion: Isomerization in $HO_2$. J Chem Phys 2010;133(10):101–5.
[119] Barnes GL, Kellman ME. Detailed Analysis of Polyad-Breaking Spectroscopic Hamiltonians for Multiple Minima with above Barrier Motion: Isomerization in $HO_2$. J Chem Phys 2011;134(7):074–108.
[120] Duval PD, Barrett BR. Quantitative description of configuration mixing in the interacting boson model. Nucl Phys A 1982;376(2):213–28.